Geological controls on fluid flow and gas hydrate pingo development on the Barents Sea margin

M. Waage[1], A. Portnov[2], P. Serov[1], S. Bünz[1], K. A. Waghorn[1], S. Vadakkepuliyambatta[1], J. Mienert[1], K. Andreassen[1]

[1]CAGE – Centre for Arctic Gas Hydrate, Environment and Climate, Department of Geosciences, UiT the Arctic University of Norway, N-9037 Tromsø, Norway

[2] School of Earth Sciences, The Ohio State University, Columbus, Ohio, USA.

Corresponding author: Malin Waage (malin.waage@uit.no)

Key Points:

- At the Barents Sea margin, several actively leaking gas-hydrate bearing pingos are seafloor manifestations of a deep sourced fluid flow system
- Gas is supplied through conduits that penetrate low permeable glacial deposits and underlying faulted rocks with abundant gas accumulations
- The shallow fluid migration is related to deep-rooted faults of the Hornsund Fault Zone

Abstract

In 2014, the discovery of seafloor mounds leaking methane gas into the water column in the northwestern Barents Sea became the first to document the existence of non-permafrost related gas hydrate pingos (GHP) on the Eurasian Arctic shelf. The discovered site is given attention because the gas hydrates occur close to the upper limit of the gas hydrate stability, thus may be vulnerable to climatic forcing. In addition, this site lies on the regional Hornsund Fault Zone marking a transition between the oceanic and continental crust. The Hornsund Fault Zone is known to coincide with an extensive seafloor gas seepage area; however, until now lack of seismic data prevented connecting deep structural elements to shallow seepages. Here we use high-resolution P-Cable 3D seismic data to study the subsurface architecture of GHPs and underlying glacial and pre-glacial deposits. The data show gas hydrates, authigenic carbonates and free gas within the GHPs on top of gas chimneys piercing a thin section of low-permeability glacial-sediments. The chimneys connect to faults within the underlying tilted and folded fluid and gas hydrate bearing sedimentary rocks. Correlation of our data with regional 2D seismic surveys shows a spatial connection between the shallow subsurface fluid flow system and the deep-seated regional fault zone. We suggest that fault-controlled Paleocene hydrocarbon reservoirs inject methane into the low-permeability glacial deposits and near-seabed sediments, forming the GHPs. This conceptual model explains the existence of climate sensitive gas hydrate inventories and extensive seabed methane release observed along the Svalbard-Barents Sea margin.

Plain Language Summary

Gas hydrates (concentrated hydrocarbon gases in cages of ice) are stable within high-pressure and low-temperature. At boundary conditions, minor increases in ocean temperature may trigger gas hydrate decay and the possibility that gas hydrates may dissociate due to future warming causes particular awareness. We present observations of a hydrate system expressed as ≤450 m wide and ≤10 m high gas hydrate pingos (seabed mounds bearing gas hydrates). The geological conditions controlling the formation of these shallow gas hydrate accumulations have not been previously investigated. Along a ~700 km region that coincides with a regional fault system, the Hornsund Fault Zone, more than 1200 seeps releasing gas from the seafloor have been observed. Linkage of this fault zone to the methane hotspots has been hypothesized but never supported by empirical data. Combining new and published data, we postulate the major preconditions for GHP development: geologically constrained focused release of methane from 55-65 million-year-old rocks, modern gas hydrate stability conditions, and a drape of muddy bottom-sediments favorable for heaving due to hydrate growth. We observe a clear relationship between this methane system and the regional fault

system, which potentially demonstrates a typical scenario of fault-controlled methane migration across the Svalbard-Barents Sea margin.

1 Introduction

Methane in gaseous, dissolved and solid (gas hydrate) form is heterogeneously distributed in the continental margins of the Arctic Ocean constituting a significant carbon source (Ruppel, 2011, Kretschmer et al., 2015, Marín-Moreno et al., 2016, Vadakkepuliyambatta et al., 2017). Methane-generation rates and variability in upward migration and sequestration into a pressure and temperature sensitive gas hydrate stability zone (GHSZ) generally control the presence in shallow subsurface. Driven by buoyancy forces and pressure gradients, gas migration along faults, fractures and inclined bedding planes is a common mechanism of relatively fast methane transfer through unlithified sediments (Cartwright, 2007, Sun et al., 2012, Vadakkepuliyambatta et al., 2013, Chand et al., 2014). Tectonic and glacial-isostatic events may reactivate fractures and faults imposing a temporal variability on spatially heterogeneous fluid flow (Andreassen et al., 2017, Fjeldskaar and Amantov, 2018, Wallmann et al., 2018).

Microbial degradation of methane in sediments (Boetius et al., 2000) and in the water column (Steinle et al., 2015) significantly minimizes methane emission to the atmosphere. Therefore, dissociation of shallow gas hydrates due to ocean warming likely supplies less methane to the atmosphere than previously assumed (Biastoch et al., 2011, Ruppel and Kessler, 2017, Vadakkepuliyambatta et al., 2017). In turn, microbial turnover of methane plays an important role for seabed ecosystems (e.g., Niemann et al., 2006). On distal shelves across the Arctic Ocean, specific methane-dependent biomass may act as an important energy source for non-methanotrophic macro and micro faunal assemblages and species (Åström et al., 2017, Sen et al., 2018).

During Quaternary glaciations, Arctic continental shelves experienced growth of the GHSZ to the depth of several hundred meters under the ice sheets (Portnov et al., 2016, Andreassen et al., 2017, Serov et al., 2017). Ice sheet retreat triggered a pressure decrease, sea level rise and warming of the seabed, causing gas hydrate dissociation and release of free gas into the water column (Portnov et al., 2016, Andreassen et al., 2017, Serov et al., 2017). This might have led to the formation of prominent seabed structures such as pockmarks (Portnov et al., 2016), craters (Solheim and Elverhøi, 1993, Lammers et al., 1995, Andreassen et al., 2017) and pingos (Serov et al., 2017) that document past gas venting.

Presently, more than 1200 methane seeps are active in 90-410 m water depth west of Svalbard (Westbrook et al., 2009, Sarkar et al., 2012, Berndt et al., 2014, Sahling et al., 2014, Mau et al., 2017). Despite previous studies of seep activity and the role of gas hydrates in modulating methane release (Westbrook et al., 2009, Thatcher et al., 2013, Berndt et al., 2014, Geissler et al., 2016, James et al., 2016), the sources and processes of gas migration and their seabed expressions along the Arctic margins are still poorly understood (Sarkar et al., 2012, Knies et al., 2018). For example, Mau et al. (2017) proposed that pathways for gas

migration on the western Svalbard margin exist along the Hornsund Fault Zone marking the transition between oceanic and continental crust (Figure 1). Assuming that methane seeps along the western Svalbard margin are confined to structural lineaments of the Hornsund Fault Zone, the fluid flow system is presumably connected to underlying hydrocarbon accumulations. However, due to the scarcity and low resolution of available seismic data (Eldholm et al., 1987; Nøttvedt et al., 1988), a connection between the structural elements with the observed fluid flow features and potential deeper reservoirs has not been observed.

Our study site (Figure 1; 360 – 390 m water depth) lies within the Hornsund Fault Zone complex in the previously glaciated Storfjordrenna (Storfjorden trough) of the NW Barents Sea (just 50 km south of Svalbard Archipelago). A shallow stratigraphic borehole 7616/11- U- 02 10 km east of the study site (Grogen et al., 1999; Lasabuda et al., 2018) confirms the presence of Palaeocene matured hydrocarbon shows (Grogan et al., 1999). The study site shows six distinctive seabed mounds, each up to 450 m in diameter and 10 m high. From seafloor ROV video transects, bottom samples and shallow (<3 m) sediment cores, it is evident that the positive topographic features consist of gas-hydrate-bearing soft cohesive muds (Serov et al., 2017). The recovery of massive gas hydrate in the soft-sediment mounds in our study area and earlier in the Beaufort Sea classified them as gas hydrate pingos (GHPs) (Paull et al., 2007, Serov et al., 2017). Pingos have been previously reported in variable environments. Ice-bearing pingos occur in areas of terrestrial and subsea permafrost due to frost heaving of water-saturated deposits (Mackay, 1998, Paull et al., 2007, Serov et al., 2015). Subsea GHPs outside permafrost regions have been documented only in a few areas: offshore Angola (Serié et al., 2012) and Nigeria (Cunningham and Lindholm, 2000), in the Joetsu Basin in the Japan Sea (Freire et al., 2011) and offshore California (Paull et al., 2008). Mutually, these studies link the formation of GHPs to gas leakage from thermogenic sources through deep-seated faults (Cunningham and Lindholm, 2000, Paull et al., 2008, Freire et al., 2011, Serié et al., 2012).

The GHPs in Storfjordrenna leak methane and heavier hydrocarbons in the form of free and dissolved gas (Hong et al., 2017). Authigenic carbonates on the seabed and in the sediments suggest that methane release has been ongoing for several thousand years (Hong et al., 2017, Serov et al., 2017). However, given sufficient water depth (380 m) and relatively low bottom-water temperature of +2°C at the study site, GHPs are presently located inside the GHSZ, yet close to its upward termination limit (Hong et al., 2017). Therefore, they are sensitive to even minor changes in the pressure-temperature field. After the discovery of the Storfjordrenna GHP field in 2014, several studies have been published on sediment and pore-water chemistry, seabed-biology and post-glacial evolution (Hong et al., 2017, Serov et al., 2017, Hong et al., 2018, Sen et al., 2018). According to coupled ice sheet and gas hydrate modelling, the gas hydrate system in the Storfjordrenna existed under subglacial conditions over a long time, i.e., at least 33 kyrs (Serov et al., 2017). After the Last Glacial Maximum (around 20 cal. ka BP) it was modulated by glacial isostatic rebound, sea level oscillations and bottom water temperature changes, eventually leading to episodic collapses and re-appearance of gas hydrates under marine conditions (Serov et al., 2017).

This study aims to improve our understanding of the fundamental geological controls on the long-living fluid flow system at Storfjordrenna. To examine this system, we acquired two high-resolution P-Cable 3D seismic datasets over a total area of ~17 km^2 covering six GHPs. We investigate the geological structures beneath the GHPs (~600 m thick sediment section below the seafloor) by mapping glacial deposits, structural lineaments, fluid accumulations, fluid flow pathways, and the internal 3D architecture of the GHPs. Existing regional geological and geophysical analyses of conventional 2D seismic profiles allow us to compare and correlate our observations within a larger geological framework. Particularly, we aim to document the linkage between the structural elements of the Hornsund Fault Zone and methane migration from potential deeper petroleum reservoirs.

2 Geological setting

The Barents Sea is a shallow epicontinental sea comprising sedimentary basins and highs (Gabrielsen et al., 1990, Faleide et al., 1991, Grogan et al., 1999). The passive continental margin of the western Barents Sea evolved during the Late Cretaceous-Middle Cenozoic continental break-up of the supercontinent Pangea and subsequent opening of the Norwegian-Greenland Sea (Myhre and Eldholm, 1988, Faleide et al., 1993). The margin consists of three segments representing different tectonic styles of continental-oceanic transition zone: a predominantly shear zone in the south (the Senja Fracture Zone), a rift zone marked by abundant Early Eocene volcanism in the middle (The Vestbakken Volcanic Province) and another predominantly shear zone in the north (the Hornsund Fault Zone) (Faleide et al., 2008). Our study area is located within a shear segment of the northern Hornsund Fault Zone, which is characterized by N-NW trending normal faults and E-W striking shear faults (Bergh and Grogan, 2003, Lasabuda et al., 2018) (Figure 2A-C). More specifically, the area covered by our high-resolution P-Cable 3D seismic is dominated by dipping westward NNW-SSE trending normal faults (Bergh & Grogan, 2003, Shlykova et al., 2008). The existing structural reconstruction (Bergh and Grogan, 2003; Shlykova et al., 2008; Lasabuda et al., 2018) is based on grids of 2D seismic profiles acquired with 10 to 30 km spacing. Tectonic lineaments demarcate a block of uplifted and substantially eroded pre-Devonian basement structure – the Sørkapp Hornsund High (Figure 2A, B). The Sørkapp Hornsund High formed in mid-late Jurassic and continued to rise throughout the middle Cenozoic (Anell et al., 2016) (Figure 2C).

Northern Barents Sea stratigraphy from Pre-Devonian to Cenozoic is uncertain due to a lack of borehole and seismic data (Faleide et al., 2008). However, existing studies suggest that Late Cretaceous to middle Cenozoic deposits lay discordantly on top of the pre-Devonian basement rocks infilling local graben structures (Grogan et al., 1999, Bergh and Grogan, 2003, Faleide et al., 2015, Anell et al., 2016) (Figure 2A, B). Peak tectonism occurred in the Oligocene, leading to NW Barents Sea margin extension and subsidence expressed in extensional structures and fault displacements along the Hornsund Fault Zone (Eldholm et al., 1987, Bergh and Grogan, 2003, Lasabuda et al., 2018). During Palaeocene-Eocene tectonism,

compression led to formation of the West Spitsbergen Fold and Thrust belt to the north of the study area, and rifting led to the development of the Vestbakken Volcanic Province in the south. In the transitional zone between the West Spitsbergen Fold and Thrust belt and the Vestbakken Volcanic Province, the Hornsund Fault Zone might show signs of compression or wrench tectonism (Grogan et al., 1999, Bergh and Grogan, 2003).

Subsequent Pliocene and Pleistocene reciprocal glacial advances and retreats led to the build-up of the upper regional unconformity (URU) on the shelf (Vorren et al., 1991) and the Storfjordrenna trough mouth fan (TMF) on the slope, progressively extending beyond the former limit of the shelf edge (Laberg and Vorren, 1996, Pedrosa et al., 2011). Hence, our study area is located at the triple junction between (1) a basement high ("Pre-Devonian rocks"), which experienced extreme Mesozoic and Cenozoic uplift and erosion, (2) a northward propagating shear zone active during Palaeocene-Pliocene (and deposition of the "the pre-glacial deposits") and (3) a depocenter of Quaternary glacigenic sedimentation (deposition of the "glacial deposits") (Figure 1 and 2).

3 Methods

Two high-resolution P-Cable 3D seismic data sets were acquired in July 2016 onboard RV *Helmer Hanssen*. Simultaneously, acoustic water column data from a multibeam EK300 was acquired to map gas flare locations in the water column.

The P-Cable 3D seismic system includes 14 streamers of 25 m length each with a streamer spacing of 12.5 m. Each streamer contains eight receiver groups with a group interval of 3.125 m. Seismic energy was generated using one GI air gun with an injector/generator volume of 737/737 cm^3, operated in harmonic mode with a pressure of 160 bar. For more information about the P-Cable system, see Planke et al. (2009) and Petersen et al. (2010). Processing was performed using RadexPro (2016) software and followed an established workflow (e.g., Petersen et al., 2010, Plaza- Faverola et al., 2015). The processing flow included de-spiking of noisy channels likely related to electrical interference (burst noise removal filter that rejected data with more than 65 % higher amplitudes than the average of the surrounding traces), geometry assignment, compensation for amplitude loss (spherical divergence), band-pass filter of 10-15-300-350 Hz, 3D binning at 6.25 x 6.25 m and NMO (Normal-Move Out) correction, median stack using water-velocity 1478 m/s and finally 3D Stolt migration (using the stacking velocity). The dataset has a dominant frequency of 117 Hz between the seafloor at ~ 490 ms and sub-seafloor at 1000 ms TWT.

The average horizontal resolution is comparable to the bin size of 6.25 m, and the average vertical resolution is calculated to be ~ 3-4 m using the Rayleigh Criterion and a seismic velocity of 1500-2000 m/s. The largest 3D seismic cube (Storfjordrenna 3D) covers an area of ~ 14 km^2 (7 x 2 km) and was acquired in a SW-NE direction (Figure 4B). GHP 1 – 5 are located in the central zone of the 3D seismic cube within a 6 km^2 surface area (Figure 4). The second 3D seismic cube (Storfjordrenna Corridor) covers ~ 3.2 km^2 (8 x 0.4 km) and was acquired in NW-SE direction, overlapping partly with Storfjordrenna 3D, and images

GHP 5 and 2 in the central part and GHP 6 in the NW part (Figure 4B). Seismic reflections are visible down to the first seafloor multiple at ~1000-1100 ms TWT. However, only weak or sporadic reflections occur beneath ~750 ms TWT.

The seismic data is of minimum phase reversed SEG Standard. Therefore, a positive amplitude (peak-over-trough) reflection (i.e. the seafloor) should represent a transition to a harder material (increase in acoustic impedance), whereas a negative amplitude (trough-over-peak) reflection represents a transition to a softer material (a decrease in acoustic impedance). The seismic data is presented in TWT as an accurate depth conversion is not feasible due to the lack of a proper velocity model. For convenience, however, some features are described in distance-depth. Based on the Hamilton (1978) scheme of sound velocity through different earth materials, we use an average velocity of 1700 m/s for the glacial deposits (assuming glacial till), and 2000 m/s for the pre-glacial deposits (assuming it is early-middle Cenozoic sandstones and shales).

We also use a number of previous geological and geophysical studies on regional geology in the area (Grogan et al., 1999, Bergh and Grogan, 2003, Dallmann, 2015, Faleide et al., 2015, Anell et al., 2016), high-resolution 2D seismic lines (collected by UiT) and conventional 2D seismic data (Figure A1, appendix) in order to investigate geological structures on larger scales, and place our study area into a regional geological framework. The high-resolution 2D seismic lines were acquired using a 100 m long streamer with 3.125 group interval and processed using a similar workflow as for the 3D data. The conventional dataset used for seismic correlation and structural framework was acquired by MAGE (Murmansk Arctic Geological Expedition) in 2005 and 2006 and previously interpreted by Shlykova et al. (2008) and Lasabuda et al. (2018). These data have a dominant frequency of 30 Hz and an average resolution of ~20 m (Lasabuda et al., 2018).

We modeled the gas hydrate stability zone using empirical data (bottom water temperature, thermal gradients, gas compositions and seafloor depth) and the theoretical hydrate stability phase boundary as estimated by the CSMHYD program (Sloan Jr and Koh, 2007). An average gas composition of 99.63 % methane, 0.36 % ethane and 0.01 % propane (as reported by Serov et al. (2017)) is used to estimate the gas hydrate phase boundary along with an assumed pore water salinity of 35 PSU. A seafloor temperature of 2℃ was used for the modeling (Hong et al., 2017, Serov et al., 2017). Considering the lack of geothermal gradient measurements at the location, three geothermal gradients; 30, 40 and 50 ℃ (Serov et al., 2017) are used to account for any possible variations in the region.

4 Results

4.1 Seismic units and GHPs

4.1.1 Deep geological structures

The deep-penetrating conventional 2D seismic data used in this study show a prominent acoustic basement high rising from ~6 km depth on the southern side of

Storfjordrenna and reaching URU close to or 3D seismic data sets (Figures 2A, 3A). Previous studies attribute this basement high to the southward expanding Pre-Devonian Sørkapp-Hornsund High (Figure 2B) (Anell et al., 2016). Based on a 2D seismic data crossing our study site, Lasabuda et al, (2018) indicate a thin succession of Palaeocene and possibly Cretaceous rocks (pre-glacial deposits) overlying the pre-Devonian basement (crystalline bedrock), involved in horst and graben structural setting (Figure 3). The seismic line connects the pre-glacial deposits in our study site with two shallow wells ~10 (7616/11-U-02)-30 km farther west, which show Paleocene and Cretaceous rocks (Grogan et al., 1999; Lasabuda et al., 2018) (Figure 3). Gabrielsen (1984) and Eldholm et al. (1987) suggest that the Hornsund Fault Zone started developing during late Cretaceous – early Cenozoic time. This may indicate that the pre-glacial deposits on top of the Pre-Devonian basement high are pre- and syn-tectonic deposits associated with development of Hornsund Fault Zone (Figures 1, 2, 3). For convenience, we labelled faults and fault blocks across the study area with letters A to E (Figure 3B). On top of the late Cretaceous-middle Cenozoic rift related deposits (~100-~500 m) at the study site, lies a thin (~50-200 m) drape of Quaternary sediments (glacial deposits) (Lasabuda et al., 2018) (Figure 2A, 3).

4.1.2 Linking seafloor pingos with deep geological structures.

GHPs 1 to 5 are grouped together in the central part of the study area, and GHP 6 is located in the NW part covered by the narrow 3D seismic corridor (Figure 4). The GHPs are comparable in size: GHP 3 and 4 reach 10 m high, and GHP 1, 2, 5 and 6 reach 7 m (Figure 4C). Generally, the GHP morphology is dome-shaped with some irregularities at the crests. The GHP shapes vary slightly, from round (GHP 2 and 6) to elongated with the longest axis in the WNW-ESE direction (GHP 1, 3 and 4). GHP 5 is slightly elongated with the long axis in the N-S direction. Annual hydroacoustic surveys between 2014-2016 revealed gas bubbles rising 200-300 m above the seafloor from the topographic summits of all GHPs except for GHP 5 (Sen et al., 2018) (Figures 4A, C).

The high-resolution 3D seismic data (Figure 4) reveal the upper part of the deep-seated horst and graben system. At various subseafloor depths (750-1000 ms), reflections are hardly visible. No to little seismic reflections exist beneath this depth also on the industry seismic data (Figures 2, 3), where most seismic energy beneath comes from seabed multiples). Hence, Lasabuda et al., (2018) interpret this transition to an indicative harder material to either the top of Cretaceous deposits or the upper part of the crystalline Pre-Devonian rocks.

Disregarding potential age, we divide the upper sediment column into two major seismo-stratigraphic units: upper glacial and lower pre-glacial deposits (Figure 4). We also show that crystalline Pre-Devonian rocks are bedded directly beneath the pre-glacial unit (Figure 4A, dashed line). A distinct high-amplitude reflection called the Upper Regional Unconformity (URU) that has been observed throughout the Barents Sea and parts of the SW Kara Sea separates Quaternary unlithified glacial and glacial-marine deposits from pre-quaternary (lithified) pre-glacial deposits (Solheim and Kristoffersen, 1984). The seismically

picked seafloor (Figure 4B) demonstrates the presence of E-W oriented mega scale glacial lineation's (MSGL) and gas hydrate pingos (GHPs) (Serov et al., 2017).

The 3D data reveal smaller (compared to regional structures) structural blocks comprising interbedded deposits on top of the deep-seated horst and graben structures (Figure 4-6, yellow coloured area). Above and between the blocks, fault-bounded sedimentary basins are filled with stratified, lower amplitude deposits (green coloured area on Figure 5 and 6).

One of the prominent structures in the 3D data coincides with the top of the deep-seated graben block B and rises from the depth beyond seismic penetration limit to approximately ~850 ms TWT (230 mbsf)) located in the NE area of the study site (Figure 5, block B). This graben structure shows a maximum dip of 25-30˚ striking in several directions (SW, NE, NW, and SSE), and bounded by horst on each side at faults A and B (Lasabuda et al., 2018). Further to the SW we observe a shallower upper termination of the deep-seated horst and graben structures occurring between the regional faults B and E, thus implying less basin infill (Bergh et al., 2003; Lasabuda et al., 2018) (Figures 5, 6). Here, the 3D seismic penetration is less (to ~200-250 ms below seafloor) compared to the north-eastern area above block B (Figure 6), likely a consequence of a thinner sedimentary unit. This "thinner" section coincide with the GHPs and seepage area (Figure 4-6).

Semi-parallel seismic reflections with bedding angle of ~20° between the blocks in this area indicate layered gently dipping strata (Figure 5, 6C and D, yellow area). The lack of coherency along the reflections, as well as a sudden change in reflection dip suggest that the blocks may be broken by listric faults. The steep 30-60° listric faults in the upper part are gentler and eventually terminate in the lower sections of the seismic cube. We apply a flatness map, which is a seismic surface attribute map to search for coherent reflection events and their dips, where 0 is 90 degrees and 1 is 0 degrees. As such, the flatness map of the upper pre-glacial deposits (from just beneath the URU reflection and 35 ms below) (Figure 6A) provides and enhances the dipping coherent reflections and fault planes that are truncated by the URU due to differentiating steep (~0) and flat (~1) events. The results show that fault planes do mostly occur at the distinct transition between coherent dipping strata (Figure 6B) and chaotic areas, or follow the same trend (Figure 6A). The fault-strike is wavy to straight across the study site with a general NNW-SSE direction. Some of the faults coincide well with the deeper identified faults A-E (as indicated in the figure 6). Fault offset varies over the study area reaching up to 50 m beneath GHP 5 and 6 (Figure 6C, blue line).

Some pingos are located directly above the large deep-seated faults. For example, GHP 4 and GHP 2, coincide with the shallow termination of the deep-seated fault B; and GHP 6, coincides with the deep-seated fault D (Figures 3, 5, 6). Pre-glacial deposits beneath GHP2 and 6 are not only folded, but show also small extensional faults that may act as fluid pathways. The observations point towards compressional stresses along pre-determined planes of weakness (extension) or faulting due to excess shear (compression) (Figures 6C, D).

4.1.3 Fault-bounded sedimentary basins

In the upper part of the pre-glacial unit, multiple low-amplitude seismic reflections fill small N-S oriented sedimentary basins bounded by the faults (Figure 5, 6C). The layered strata have a slightly wedge-shaped internal structure with upward drags towards the fault-bounded margins.The deepest observed basin (up to ~1050 ms TWT) occurs above the graben named block B and west of the horst structure bounded by fault A (Figure 3, 5). Three to five traceable reflections separated by low amplitude semi-transparent sub-units form the lowermost graben-fill (Figure 5). The graben-fill dips to the southwest where it laterally increases in thickness to a total of ~ 300 m close to fault B (Figures 3, 5). On top, another set of prominent sub-parallel reflections occurs (Figure 8, NE area) , however, proximal to Fault B the reflections have a dominating tilt towards NE. These strata appear to bend upward and terminate at the URU. Another relatively large basin is located further SW and is ~370 m wide, 970 m long and ~50 m deep (marked basin fill A2 (A2, Appenidx) in Figure 6D) with GHP 1, 2 and 4 located on its margins (Figure 6 B, sedimentary basin).

The thickness variations, common wedge-shaped asymmetry, on-lapping towards the fault-walls indicate that these sedimentary basins have syn-tectonic nature. Additionally, the sedimentary sequences appear to have a synformal bend-like structure at or near fault B, in otherwise sub-parallel configuration, implying some dragging of the sediment along the fault plane. We suggest that parts of the pre-glacial deposits directly underneath the URU consist of sediments filling the accommodation space created by extensional faulting associated with the development of the Hornsund Fault Zone (Prosser, 1993, Grasemann et al., 2005).

4.1.4 Glacial deposits

The glacial deposits comprise a 35-150 m (40-170 ms TWT) thick sediment section with groups of sub-horizontal, continuous high-amplitude seismic reflections represented by surfaces SR1-SR4 and the URU (Figure 7). The surfaces are separated by acoustically semi-transparent intervals (Figure 7B). The horizons (SR1-4) truncate weak reflections within the semi-transparent intervals suggesting that the surfaces may be erosive. Surfaces SR1, SR3, and SR4 are not developed across the entire study area; they taper out in the northern part where the glacial unit thins (Figure 7B, C). The URU has a more pronounced relief than the overlying glacial-related surfaces. The underlying geological structures appear to influence the URU topography. All interpreted surfaces dip slightly towards the south-southwest and are characterized by the appearance of distinct glacial features such as lineations (on all surfaces) and transverse ridges (on surface SR4) (Figure 7C). The lineations have a similar principal ENE-WSW orientation, parallel to the northern flank of the cross-shelf trough and match well with the orientation of modern glacial bedforms on the seafloor (Figure 7A). The lineations termed megascale glacial lineations (MSGLs) are therefore inferred to be formed by fast-flowing ice streams (e.g., Winsborrow et al., 2010). The variations in roughness (Figure 7C) between the surfaces may indicate differences in ice-stream characteristics or

better preservation of small-scale morphology on the younger reflection surface (i.e., SR2 compared to the URU).

4.2 Fluid flow indicators

4.2.1 Acoustic anomalies and fluid indicators in the pre-glacial deposits

In the seismic data, the upper part of the pre-glacial deposits shows multiple negative (trough-over-peak) high-amplitude reflections indicating a transition to a unit with a lower acoustic impedance (Figure 8, location in figure 6 C and D). These amplitude anomalies tend to occur along steep lineaments or in the interior of the tilted blocks truncated by the URU. GHPs 1, 2, 3, 4 and 6 are located above such blocks showing enhanced reflections in their apexes just beneath the URU, whereas GHP 5 does not correlate with any prominent basement structure (Figures 5, 6D). The scattered character of seismic amplitude anomalies along the coherent reflections may suggest that the lower impedance material is caused by gas within the pore space and fractures rather than lithology changes.

In the area below the GHPs, we observe a scattered, patchy seismic trough-over-peak reflection that mimmicks the seafloor and cross-cuts the dipping pre-glacial (pre-tectonic) deposits (Figure 9). These observations indicate that this seismic feature occurring between 85 and 150 mbsf (average of 114 mbsf) represents a bottom simulating reflection (BSR) (Shipley et al., 1979). A BSR is a seismic indicator of the boundary between the underlying gas- or water-bearing sediments and the overlying hydrate-bearing sediments (Shipley et al., 1979). The presence of a prominent BSR and abundant seismic high amplitude anomalies below strongly suggests that the pre-glacial deposits accommodate shallow gas and hydrate accumulations.

In the absence of geothermal gradient measurements, any modeling of the GHSZ in the study area will remain vague. Given the plausible temperature gradient range of 30-50 °C/km for the West Barents Sea margin, gas composition of 99.63 % methane, 0.36 % ethane and 0.01 % propane, and bottom water temperature 2 °C (Serov et al., 2017), the depth range for the bottom of GHSZ varies from 61 to 160 mbsf. Based on the observed seismic BSR depth, the estimated geothermal gradient in our study area is approximately 35 °C/km.

4.2.2 Acoustic anomalies and indications of fluid migration in the glacial deposits

GHPs are located above prominent sub-vertical zones of acoustic masking (Figures 8, 10D-F). A semi-transparent zone is also present in the sediment section below the inactive GHP 5, yet it is significantly less pronounced (Figure 10D, F). The acoustic masking zones

underneath the active pingos crosscut the entire glacial deposits and extend deep into the pre-glacial deposits (Figures 6 C and D). Beneath the GHP 3, the URU is not distorted (Figure 10E), however, it is completely wiped out and distorted in the subsurface of GHP 1 (Figure 10F). These observations indicate that distortions as well as pure amplitude loss occur. There is no acoustic masking immediately below the high amplitude anomaly of GHP 5, however at ~560 ms depth, a bright spot appears along a topographic high of a glacial surface. We suggest that the bright spot (Figure 10F) indicates an area of isolated free gas or gas hydrate. Directly beneath this bright spot along the URU, a zone of circular acoustic masking occurs. Similar areas of acoustically masked distortion have been previously interpreted as gas chimneys – gas-charged fluid migration conduits documented in various geological settings (Gay et al., 2006, Cathles et al., 2010, Hustoft et al., 2010, Plaza- Faverola et al., 2010). A minor fraction of free gas (1%) in the pore space of sediments is sufficient to decrease compressional wave velocities and blur acoustic impedance contrast of layered strata producing a zone of signal blanking in form of a chimney (e.g., Tóth et al., 2014). Observations of seabed gas release, the recovery of gas hydrates within the GHPs and the results of gas sampling in sediments and the water column (Serov et al., 2017), indicate focused seafloor gas release from the shallow sediments. Alternatively, acoustic masking zones without significant distortion can be caused by a sharp impedance contrast (high amplitude anomalies) directly below the GHPs. The short offset of the P-Cable acquisition system in relation to the GHPs suggest that such shadow effect is also plausible. We suggest that these sub-vertical zones of acoustic masking underneath the pingos may be caused by a combination of both effects, however, from now on we refer to them as gas chimneys - gas-charged fluid migration pathways.

Several seismic pull-up events are observed in the glacial deposits beneath the inactive GHP 5 (Figure 10F), and below these events, the bright spot mentioned above appears. Such effects are not clearly observed beneath the other GHPs (i.e., beneath GHP 3 and 1, Figure 10E, F). However, some pull-up effects seem to exist beneath GHP 3 (Figure 10E), and otherwise, the gas chimneys underlying the active GHPs may mask other seismic expressions such as glacial horizons and pull-ups. Pull-up events may be caused by higher-velocity substances in the strata above and may result from the presence of authigenic carbonates or gas hydrates within the pingos (Madof, 2018).

4.2.3 Acoustic anomalies and fluid migration indicators within the GHPs

The GHPs at the study site are all characterized by internal chaotic high-amplitude reflections, lacking a prominent basal reflection corresponding to the seafloor (Figures 6C, D, 8). The seafloor surface shows a variation in seismic amplitude with depth and topography, however not exclusively related to the location of GHPs, which could suggest a different seafloor material compared to the surrounding sediments. Brightening of the amplitudes occur on elevations, including ridges of the MSGL, and crests of GHPs (Figure 10B). For example, the crest of the most elevated GHP 4 shows anomalously high amplitudes, while the

crest of GHP 3 located in deeper water shows no amplitude difference compared to the surrounding seafloor. These variations in the seafloor acoustic impedance may indicate variable lithology of the bottom sediments. Finer grained, acoustically softer sediments might fill troughs and topographic lows, whereas more compacted sediments as well as exposed carbonates and gas hydrates are likely to be dominant on the highs and shallower parts due to erosion by bottom currents (e.g., Bellec et al., 2009).

The internal reflections of the GHPs occurring beneath the seafloor are characterized by several chaotic reflections that breach at the summit of the GHPs (Figures 8, 10 E, F). The uppermost of these reflections appear mostly as a trough-over-peak reflection of anomalously high amplitude along the active GHPs (all except GHP 5) (Figure 8, 10 E, F). The presence of pull-up events beneath GHP 5, however, strongly indicate that the high amplitude anomaly should be a peak-over-trough reflection, representing an increase in acoustic impedance. However, depending on the size of these features, and resolution of the seismic data, we expect some heterogeneity within the pingos where small-scale variation in cementation, gas content, hydrate and carbonates, could explain the apparent polarity variations and amplitude changes across the GHPs.

We suggest that amplitude anomalies within GHPs 1, 2, 3, 4 and 6 indicate gas, gas hydrate (also evident from shallow cores), carbonate crusts (observed on seafloor) or alternation-cementation (e.g., Greinert et al., 2001). This effect is well documented, and is widely observed underneath pockmarks and within vertical fluid conduits such as gas chimneys (e.g Wenau, et al. 2017). Based on gas hydrate recoveries and video surveys (Hong et al., 2017, Sen et al., 2018) it is possible that segments of these mounds accommodate gas hydrate veins or authigenic carbonate formations. Pure gas hydrates and authigenic carbonates have an anomalously high acoustic velocity of ~3300 m/s (Lee et al., 1996) compared to up to ~1700 m/s for the surrounding glacial sediments. During the multiple field campaigns in 2014-2016, GHP 5 did not show any gas-induced hydroacoustic anomalies in the water column, which is in good agreement with the lack of seismic indications of free gas in the shallow subsurface of this GHP (Hong et al., 2017, Serov et al., 2017, Sen et al., 2018) (Figure 6D, 8B)

5 Discussion

5.1 Potential tectono-stratigraphic controls on gas hydrate pingo formations

Accurate detection and mapping of fault systems, gas migration conduits, and gas hydrate reservoirs require 3D seismic technologies e.g., (Bünz et al., 2005, Hustoft et al., 2007, Sultan et al., 2007, Hornbach et al., 2008). To our knowledge, GHPs were investigated using 3D seismic method only once prior to this study, - offshore Angola (800-1000 m water depth) (Serié et al., 2012). There, a cluster of similar mounds is attributed to a gas migration system along the flanks of a salt diapir (Serié et al., 2012). GHPs at the NW Barents Sea

margin are not associated with salt tectonics and show different geological controls. Our 3D seismic observations and interpretations of shallow geological structures connect to the regional complex fault system at the oceanic-continental crust transition. The upper termination of these faults and structural highs that coincide with the fault zone further match with the locations of seafloor seepage. The shallow stratigraphic borehole 7616/11- U- 02 10 km east of the study site (Figure 3, Grogen et al., 1999; Lasabuda et al., 2018) confirms the presence of Palaeocene source and reservoir rocks, which we correlate to our study area (Grogan et al., 1999). This suggests that possible Paleocene fault-controlled hydrocarbon plays (and source rocks) are responsible for charging the GHPs with free gas through the faulted network and overlying chimneys within the upper glacial deposits. A relationship between this local fluid flow- and a regional fault system potentially demonstrates a scenario for fault-controlled methane migration, which may also occur regionally along the broader Svalbard-northwestern Barents Sea margin, including the ~700 km trending zone of widespread natural seafloor gas release (Mau et al., 2017).

Although seafloor seepage is widespread along the HFZ, there are many places along the fault zone where gas seepage is absent. There are several factors, which make our study area different from its near surroundings. For example, the 2D seismic correlation suggests that the regional R1 reflection represents the base of the regional middle Pleistocene GIII glacial deposits (Figure 2A). Therefore, the glacial deposits are suggested to comprise the middle-late Pleistocene succession generated by repeated glaciations during the last 0.4 Ma. At our study site located within the Sørkapp-Hornsund High, only a thin (~35-150 m) drape of Pleistocene low-permeability glacial sediments exists. The TMF, which has accumulated products of glacial erosion from the shelf, drastically thickens outside the Sørkapp-Hornsund High westward and southward along the fault zone (Eldholm et al., 1987, Amundsen et al., 2011, Rebesco et al., 2014) (Figure 1), causing a thicker seal, which may hinder gas release over a large area (Figure 2). Furthermore, it is a depocenter of postglacial sedimentation of cohesive, soft muds (Rasmussen et al., 2007) favourable for deformation, gas hydrate growth and carbonate precipitation. Lastly, this is as far as we know the only place in the Barents Sea where gas hydrates occur in the glacial/Quaternary sediments. The conjunction of geologically controlled methane flow, stable gas hydrates, and deformable superficial sediments is a rare combination across the Barents Sea shelf, which allows for formation of gas hydrate pingos. Other known seep sites at similar physiographic position typically occur within glacial tills (Roy et al., 2015), or lithified rocks (Andreassen et al., 2017) less prone to seabed heaving.

Indeed, pockmarks and craters are much more common seafloor expressions of seepage in both, soft and harder sediments (e.g. King et al., 1970; Hovland, 1981; Petersen et al., 2008, Waghorn et al., 2018). Thus, in addition to sediment characteristics, other parameters such as quantity of gas supply and gas hydrate growth dynamics likely play equally important roles in forming gas hydrate pingos. Several studies (e.g. Sultan et al., 2010, Andreassen et al., 2017) suggest that seafloor elevation might as well be a precursor to seafloor depression formation. A continued high flux of methane is required to maintain high methane concentrations preventing dissolution of hydrates and gas hydrate pingo collapse

(e.g., Kvenvolden and McMenamin, 1980, Hovland and Svensen, 2006, Serié et al., 2012). Serie et al. (2012) suggest that difference in morphology of GHPs along the Angolan continental margin reflects different development stages and seepage activity. Steeper dipping and taller GHPs indicate recent or prolonged growth of structures whereas small structures with less distinct topography are older. At Storfjordrenna, GHP 1 and 5 are the least elevated structures which show little or no seepage (Serov et al., 2017), pointing towards a possible connection between shape of pingos and methane flux.

Hong et al., 2017 showed that GHPs in Storfjordrenna have not experienced gas hydrate dissociation due to seasonal or long-term warming of bottom waters. Along with an inferred long history of gas release, the thermogenic nature of gas (Serov et al., 2017), and documented deep-rooted fluid flow pathways suggests that modern climate warming does not necessarily initiate methane release at Storfjordrenna GHPs, but instead it has been a component of a long-living self-sustainable Arctic fluid flow system.

5.2 Sources of migrating gas

We suggest that the Palaeocene sedimentary rocks may act as both source rocks and an intermediate trap for hydrocarbon gases (Figures 3). Give an up to 3 km Cenozoic net erosion (Henriksen et al., 2011, Laberg et al., 2012), it is plausible that hydrocarbons matured in-situ in the pre-glacial strata at a time of deeper burial (oil generation window starts at ~2 km, whereas gas generation window at ~3 km burial). Alternatively, the fluids might migrate laterally from surrounding sources (for example from west or south (Figure 2) where the sedimentary basin deepens, allowing Cenozoic rocks to undergo deeper burial conditions (e.g., Faleide et al., 2015). By the end of Palaeocene (~56 Ma ago) during the pre-glacial deposition, the NW Barents Sea and Svalbard region were a shallow-water continental shelf with fluvial and deltaic settings. This environment hosted swampy wetlands favorable for percipitation of massive peat layers that evolved into the Firkanten coal units, which are widely distributed on Svalbard (Ingolfsson, 2004). Coal formations are assoicated with light hydrocarbon gasses. On Svalbard, significant amount of wellhead gas is normally released during drilling the Firkanten coal seams (Elvevold et al., 2007). We therefore speculate that the gasses at our study site might originate from Paleocene coal seams below or in close proximity to the GHPs.

Similar conditions may exist along other segments of the Hornsund Fault Zone, explaining the high intensity of natural seafloor seeps documented along this Arctic Continental margin (Mau et al., 2017). Comparable hydrocarbon leakage through extensional deep-seated faults from various hydrocarbon systems is widespread in the Barents Sea. For example, only in the south-western Barents Sea open for petroleum exploration, subsurface fluid flow features are known to be associated with deep-seated faults over an area of several thousand km^2 (Vadakkepuliyambatta et al., 2013).

5.3 Evolution of the fluid flow system in Storfjordrenna

The pre-glacial- and glacial deposits document different sets of features related to fluid flow and gas hydrate accumulations. Within the Palaeocene strata of the pre-glacial deposits, a patchy BSR indicates the boundary between water or free gas and gas hydrates at the base of GHSZ (Figure 9). Additionally, numerous trough-over-peak high amplitude anomalies in the pre-glacial deposits indicate a change to a lower impedance material, such as dispersed free gas accumulations within pore spaces in a permeable matrix (Figures 6 C, 7). This would suggest fluid flow along inclined and folded permeable layers as well as along the major faults (Figure 5, 6).

In contrast with the pre-glacial deposits, showing widespread fluid and gas hydrate indications, the glacial deposits show narrow zones of vertical acoustic masking - gas chimneys, indicating focused fluid migration pathways. The subsurface of GHP 5 does not show evidence of shallow faults or dipping Cenozoic strata, but instead it appears that older rocks locally outcrop here, which might explain the lack of seepage indicators in the water column and subsurface of GHP 5 (Figure 6, 10). However, the presence of a GHP itself is a clear evidence of past fluid flow or seepage. An elongated ridge with high-amplitude anomalies exists along the URU (Figure 6B) and strikes just beneath GHP1 and GHP5. If this positive feature contains permeable deposits, it would enable fluid migration and capturing along the ridge, which might have eventually led to the fluid outbursts that have developed in GHP5.

The distinctly different patterns and indications of fluid flow features in the pre-glacial and glacial deposits suggest that the pre-glacial deposits have better reservoir qualities, while the glacial deposits likely act as a seal with relatively low permeability outside of the chimney areas. Within our study site, seismic chimneys originate from apexes of inclined bedrocks-basement blocks truncated by the URU (Figure 6, 10) and terminate at GHPs suggesting that they transport fluids through low permeability glacial deposits. None of the chimneys appears to be connected to the graben-like depressions between the blocks infilled with syn-rift deposits. The chimneys exist only in connection with GHPs and not elsewhere. The GHPs are located on top of seismic features that we interpret as gas hydrates and methane-derived authigenic carbonates (Figure 10). Recovered hydrate-bearing sediments in 1.5 – 3.5 m long cores demonstrate veins and lenses of massive gas hydrates in fine-grained hemipelagic sediments as well as abundant carbonate formations (Serov et al., 2017). Gas hydrates are also known to expand within pore spaces and fractures as they form. We suggest that propagation of shallow fractures induced by pressurized fluids and their subsequent plumbing with gas hydrate may be a possible scenario. Active upward migration of free gas that accumulates as gas hydrates in the shallow sub-surface causes a reduction in density and an increase in volume of the soft cohesive muddy sediments, which due to buoyancy effects support swelling and the upward movement of gas-hydrate hosted strata. Such process is postulated to contribute to gas hydrate pingo growth (e.g., Serié et al., 2012, Somoza et al., 2014). The upward bends of normal reflections observed further down in the stratigraphy below GHP 5 and 3, however, is more likely to represent velocity pull-ups, since one would expect a clearer seismic signature of such "gas hydrate swelling" in the sedimentary column, similar to the high amplitudes and fractures visible in the pingos.

Based on our structural and seismo-stratigraphic analyses, we propose a set of factors, which initiate and modulate the free gas and gas hydrate system at the Storfjordrenna GHP field (Figure 11):

1. Extreme Quaternary glacial erosion up to 3 km (Henriksen et al., 2011) caused a significant emergence of deeper rocks, which may represent both source rocks or/and intermediate hydrocarbon traps;

2. Permeable inclined bedding planes and numerous deep-rooted normal faults above a pre-Devonian basement high provide conduits for vertical and lateral fluid migration.

3. Low permeability glacial deposits formed a seal on top of the fractured - pre-glacial unit, which likely hosts variating amounts of gas. This allowed accumulation of fluids below the URU. Continued migration and accumulation of gas until pressure exceeded critical value break the thin seal initiating gas chimney generation. The change in pressure gradients related to ice-sheet build up and retreat (i.e., subsidence, uplift, erosion, and gas hydrate accumulation and dissociation) might have contributed to this process.

4. Free gas migrated to the seafloor through gas chimneys forming gas hydrates in superficial sediments. Due to hydrate growth, the sediments bulk density decreased and they expanded forming gas hydrate pingos on the seafloor. Precipitation of methane-derived authigenic carbonates contributed to pingo growth. Free gas continues to flow intensely through small-scale fractures.

6 Conclusions

We have analysed high-resolution P-Cable 3D seismic data from the mouth of Storfjordrenna, 50 km south of Svalbard, where vigorous gas seepage was documented above six Gas Hydrate Pingos (GHPs). The GHPs are elevated mounds in water depths of 360-390 m reaching a height of up to 10 m above the seafloor and are up to 450 m wide. Current thermobaric conditions at these depths maintain stable gas hydrates. Here, GHPs consist of sediments bearing gas hydrate and authigenic carbonates. Video transects and sediment sampling at GHPs confirm the presence of massive gas hydrates and authigenic carbonates. Below the GHPs, our high-resolution seismic data reveal vertical, focused fluid flow structures - gas chimneys- piercing through the thin (35-150 m) section of Pleistocene glacigenic/glaciomarine sediments that forms a seal in the study area. These gas chimneys represent the upper part of a deeper-rooted gas venting system. The chimneys connect to well-defined fractures and faults within the underlying tilted and folded Paleocene sedimentary rocks down to 100-500 m below seafloor. Furthermore, conventional 2D seismic data show that these faults link to an even a deeper-seated (2-5 km) regional fault system of the Hornsund Fault Zone. The early Cenozoic sedimentary rocks show indications of gas-saturated fluids and gas hydrates as evidenced from high-amplitude reflection anomalies and a patchy bottom-simulating reflector. A spatial interconnection exists between shallow gas-

hydrate bearing seafloor mounds, underlying gas chimneys that extend downward through glacial sediments to up-dipping pre-glacial rocks, and the 2-5 km deep fault system of the Hornsund Fault Zone. We suggest that fault-controlled Paleocene hydrocarbon plays have been responsible for charging the GHPs with free gas for thousands of years, supporting widespread natural seafloor gas release at formerly glaciated Arctic continental margins such as the Storfjordrenna gas hydrate pingo field. Glacial cycles controlling subsurface pore pressure regime and thus GHSZ evolution, are further likely to have controlled activity of the fluid flow system (Serov et al., 2017).

Acknowledgments, Samples, and Data

Appendix
The appendix data presents two figures (A1 and A2).

References

Amundsen, I. M. H., M. Blinova, B. O. Hjelstuen, R. Mjelde, and H. Haflidason. 2011, The Cenozoic western Svalbard margin: sediment geometry and sedimentary processes in an area of ultraslow oceanic spreading. Marine Geophysical Research, **32**, no. 4,441-453.

Andreassen, K., A. Hubbard, M. Winsborrow, H. Patton, S. Vadakkepuliyambatta, A. Plaza-Faverola, E. Gudlaugsson, P. Serov, A. Deryabin, and R. Mattingsdal. 2017, Massive blow-out craters formed by hydrate-controlled methane expulsion from the Arctic seafloor. Science, **356**, no. 6341,948-953.

Anell, I., J. Faleide, and A. Braathen. 2016, Regional tectono-sedimentary development of the highs and basins of the northwestern Barents Shelf. Norsk Geologisk Tidsskrift, **96**,27-41.

Bellec, V. K., M. F. Dolan, R. Bøe, T. Thorsnes, L. Rise, L. Buhl-Mortensen, and P. Buhl-Mortensen. 2009, Sediment distribution and seabed processes in the Troms II area-offshore North Norway. Norwegian Journal of Geology/Norsk Geologisk Forening, **89**.

Bergh, S. G., and P. Grogan. 2003, Tertiary structure of the Sørkapp-Hornsund Region, South Spitsbergen, and implications for the offshore southern extension of the fold-thrust Belt. Norwegian Journal of Geology/Norsk Geologisk Forening, **83**, no. 1.

Berndt, C., T. Feseker, T. Treude, S. Krastel, V. Liebetrau, H. Niemann, V. J. Bertics, I. Dumke, K. Dünnbier, and B. Ferré. 2014, Temporal constraints on hydrate-controlled methane seepage off Svalbard. Science, **343**, no. 6168,284-287.

Biastoch, A., T. Treude, L. H. Rüpke, U. Riebesell, C. Roth, E. B. Burwicz, W. Park, M. Latif, C. W. Böning, and G. Madec. 2011, Rising Arctic Ocean temperatures cause gas hydrate destabilization and ocean acidification. Geophysical Research Letters, **38**, no. 8.

Boetius, A., K. Ravenschlag, C. J. Schubert, D. Rickert, F. Widdel, A. Gieseke, R. Amann, B. B. Jørgensen, U. Witte, and O. Pfannkuche. 2000, A marine microbial consortium apparently mediating anaerobic oxidation of methane. Nature, **407**, no. 6804,623.

Bünz, S., J. Mienert, P. Bryn, and K. Berg. 2005, Fluid flow impact on slope failure from 3D seismic data: a case study in the Storegga Slide. Basin Research, **17**, no. 1,109-122.

Cartwright, J. 2007, The impact of 3D seismic data on the understanding of compaction, fluid flow and diagenesis in sedimentary basins. Journal of the Geological Society, **164**, no. 5,881-893.

Cathles, L., Z. Su, and D. Chen. 2010, The physics of gas chimney and pockmark formation, with implications for assessment of seafloor hazards and gas sequestration. Marine and petroleum Geology, **27**, no. 1,82-91.

Chand, S., J. Knies, S. Baranwal, H. Jensen, and M. Klug. 2014, Structural and stratigraphic controls on subsurface fluid flow at the Veslemøy High, SW Barents Sea. Marine and Petroleum Geology, **57**,494-508.

Cunningham, R., and R. M. Lindholm. 2000, AAPG Memoir 73, Chapter 8: Seismic Evidence for Widespread Gas Hydrate Formation, Offshore West Africa.

Dallmann, W. K. 2015, Geoscience Atlas of Svalbard: Norsk polarinstitutt.

Eldholm, O., J. I. Faleide, and A. M. Myhre. 1987, Continent-ocean transition at the western Barents Sea/Svalbard continental margin. Geology, **15**, no. 12,1118-1122.

Elvevold, S., W. Dallmann, and D. Blomeier. 2007, Geology of Svalbard.

Faleide, J., S. Gudlaugsson, O. Eldholm, A. Myhre, and H. Jackson. 1991, Deep seismic transects across the sheared western Barents Sea-Svalbard continental margin. Tectonophysics, **189**, no. 1-4,73-89.

Faleide, J. I., K. Bjørlykke, and R. H. Gabrielsen. 2015, Geology of the Norwegian continental shelf, Petroleum Geoscience: Springer. 603-637.

Faleide, J. I., F. Tsikalas, A. J. Breivik, R. Mjelde, O. Ritzmann, O. Engen, J. Wilson, and O. Eldholm. 2008, Structure and evolution of the continental margin off Norway and the Barents Sea. Episodes, **31**, no. 1,82-91.

Faleide, J. I., E. Vågnes, and S. T. Gudlaugsson. 1993, Late Mesozoic-Cenozoic evolution of the south-western Barents Sea in a regional rift-shear tectonic setting. Marine and Petroleum Geology, **10**, no. 3,186-214.

Fjeldskaar, W., and A. Amantov. 2018, Effects of glaciations on sedimentary basins. Journal of Geodynamics, **118**,66-81.

Freire, A. F. M., R. Matsumoto, and L. A. Santos. 2011, Structural-stratigraphic control on the Umitaka Spur gas hydrates of Joetsu Basin in the eastern margin of Japan Sea. Marine and Petroleum Geology, **28**, no. 10,1967-1978.

Gabrielsen, R. H., R. B. Faerseth, and L. N. Jensen. 1990, Structural Elements of the Norwegian Continental Shelf. Pt. 1. The Barents Sea Region: Norwegian Petroleum Directorate.

Gay, A., M. Lopez, P. Cochonat, M. Séranne, D. Levaché, and G. Sermondadaz. 2006, Isolated seafloor pockmarks linked to BSRs, fluid chimneys, polygonal faults and stacked Oligocene–Miocene turbiditic palaeochannels in the Lower Congo Basin. Marine Geology, **226**, no. 1-2,25-40.

Geissler, W. H., A. C. Gebhardt, F. Gross, J. Wollenburg, L. Jensen, M. C. Schmidt-Aursch, S. Krastel, J. Elger, and G. Osti. 2016, Arctic megaslide at presumed rest. Scientific reports, **6**,38529.

Grasemann, B., S. Martel, and C. Passchier. 2005, Reverse and normal drag along a fault. Journal of Structural Geology, **27**, no. 6,999-1010.

Greinert, J., G. Bohrmann, and E. Suess. 2001, Gas hydrate- associated carbonates and methane- venting at Hydrate Ridge: classification, distribution, and origin of authigenic lithologies. Natural gas hydrates: Occurrence, distribution, and detection,99-113.

Grogan, P., A.-M. Østvedt-Ghazi, G. Larssen, B. Fotland, K. Nyberg, S. Dahlgren, and T. Eidvin. 1999, Structural elements and petroleum geology of the Norwegian sector of the northern Barents Sea. Paper read at Geological Society, London, Petroleum Geology Conference series.

Hamilton, E. L. 1978, Sound velocity–density relations in sea- floor sediments and rocks. The journal of the Acoustical Society of America, **63**, no. 2,366-377.

Henriksen, E., H. Bjørnseth, T. Hals, T. Heide, T. Kiryukhina, O. Kløvjan, G. Larssen, A. Ryseth, K. Rønning, and K. Sollid. 2011, Uplift and erosion of the greater Barents Sea: impact on prospectivity and petroleum systems. Geological Society, London, Memoirs, **35**, no. 1,271-281.

Hong, W.-L., M. E. Torres, J. Carroll, A. Crémière, G. Panieri, H. Yao, and P. Serov. 2017, Seepage from an arctic shallow marine gas hydrate reservoir is insensitive to momentary ocean warming. Nature communications, **8**,15745.

Hong, W. L., M. Torres, A. Portnov, M. Waage, B. Haley, and A. Lepland. 2018, Variations in gas and water pulses at an Arctic seep: fluid sources and methane transport. Geophysical Research Letters.

Hornbach, M. J., D. M. Saffer, W. S. Holbrook, H. J. Van Avendonk, and A. R. Gorman. 2008, Three-dimensional seismic imaging of the Blake Ridge methane hydrate province: Evidence for large,

concentrated zones of gas hydrate and morphologically driven advection. Journal of Geophysical Research: Solid Earth, **113**, no. B7.

Hovland, M. (1981). Characteristics of pockmarks in the Norwegian Trench. Marine Geology, 39(1-2), 103-117.

Hovland, M., and H. Svensen. 2006, Submarine pingoes: Indicators of shallow gas hydrates in a pockmark at Nyegga, Norwegian Sea. Marine Geology, **228**, no. 1-4,15-23.

Hustoft, S., S. Bünz, and J. Mienert. 2010, Three- dimensional seismic analysis of the morphology and spatial distribution of chimneys beneath the Nyegga pockmark field, offshore mid- Norway. Basin Research, **22**, no. 4,465-480.

Hustoft, S., J. Mienert, S. Bünz, and H. Nouzé. 2007, High-resolution 3D-seismic data indicate focussed fluid migration pathways above polygonal fault systems of the mid-Norwegian margin. Marine Geology, **245**, no. 1-4,89-106.

Ingolfsson, O. 2004, Outline of the geography and geology of Svalbard. University of Iceland and UNIS.

James, R. H., P. Bousquet, I. Bussmann, M. Haeckel, R. Kipfer, I. Leifer, H. Niemann, I. Ostrovsky, J. Piskozub, and G. Rehder. 2016, Effects of climate change on methane emissions from seafloor sediments in the Arctic Ocean: A review. Limnology and Oceanography, **61**, no. S1.

King, L. H., & MacLEAN, B. R. I. A. N. (1970). Pockmarks on the Scotian shelf. Geological Society of America Bulletin, 81(10), 3141-3148.

Knies, J., M. Daszinnies, A. Plaza-Faverola, S. Chand, Ø. Sylta, S. Bünz, J. E. Johnson, R. Mattingsdal, and J. Mienert. 2018, Modelling persistent methane seepage offshore western Svalbard since early Pleistocene. Marine and Petroleum Geology, **91**,800-811.

Kretschmer, K., A. Biastoch, L. Rüpke, and E. Burwicz. 2015, Modeling the fate of methane hydrates under global warming. Global Biogeochemical Cycles, **29**, no. 5,610-625.

Kvenvolden, K. A., and M. A. McMenamin. 1980, Hydrates of natural gas: a review of their geologic occurrence.

Laberg, J., and T. Vorren. 1996, The glacier-fed fan at the mouth of Storfjorden trough, western Barents Sea: a comparative study. Geologische Rundschau, **85**, no. 2,338-349.

Laberg, J. S., K. Andreassen, and T. O. Vorren. 2012, Late Cenozoic erosion of the high-latitude southwestern Barents Sea shelf revisited. Bulletin, **124**, no. 1-2,77-88.

Lammers, S., E. Suess, and M. Hovland. 1995, A large methane plume east of Bear Island (Barents Sea): implications for the marine methane cycle. Geologische Rundschau, **84**, no. 1,59-66.

Lasabuda, A., J. S. Laberg, S.-M. Knutsen, and P. Safronova. 2018, Cenozoic tectonostratigraphy and pre-glacial erosion: A mass-balance study of the northwestern Barents Sea margin, Norwegian Arctic. Journal of Geodynamics.

Lee, M., D. Hutchinson, T. Collett, and W. P. Dillon. 1996, Seismic velocities for hydrate- bearing sediments using weighted equation. Journal of Geophysical Research: Solid Earth, **101**, no. B9,20347-20358.

Mackay, J. 1998, Pingo growth and collapse, Tuktoyaktuk Peninsula area, western Arctic coast, Canada: A long-term field study. Géographie physique et Quaternaire, **52**, no. 3,271-323.

Madof, A. S. 2018, Gas hydrates in coarse-grained reservoirs interpreted from velocity pull up: Mississippi Fan, Gulf of Mexico. Geology, **46**, no. 6,559-562.

Marín-Moreno, H., M. Giustiniani, U. Tinivella, and E. Piñero. 2016, The challenges of quantifying the carbon stored in Arctic marine gas hydrate. Marine and Petroleum Geology, **71**,76-82.

Mau, S., M. Römer, M. E. Torres, I. Bussmann, T. Pape, E. Damm, P. Geprägs, P. Wintersteller, C.-W. Hsu, and M. Loher. 2017, Widespread methane seepage along the continental margin off Svalbard-from Bjørnøya to Kongsfjorden. Scientific reports, **7**,42997.

Myhre, A. M., and O. Eldholm. 1988, The western Svalbard margin (74–80 N). Marine and Petroleum Geology, **5**, no. 2,134-156.

Niemann, H., T. Lösekann, D. De Beer, M. Elvert, T. Nadalig, K. Knittel, R. Amann, E. J. Sauter, M. Schlüter, and M. Klages. 2006, Novel microbial communities of the Haakon Mosby mud volcano and their role as a methane sink. Nature, **443**, no. 7113,854.

Nøttvedt, A., L. Berglund, E. Rasmussen, and R. Steel. 1988, Some aspects of Tertiary tectonics and sedimentation along the western Barents Shelf. Geological Society, London, Special Publications, **39**, no. 1,421-425.

Paull, C. K., W. R. Normark, W. Ussler III, D. W. Caress, and R. Keaten. 2008, Association among active seafloor deformation, mound formation, and gas hydrate growth and accumulation within the seafloor of the Santa Monica Basin, offshore California. Marine Geology, **250**, no. 3-4,258-275.

Paull, C. K., W. Ussler, S. R. Dallimore, S. M. Blasco, T. D. Lorenson, H. Melling, B. E. Medioli, F. M. Nixon, and F. A. McLaughlin. 2007, Origin of pingo- like features on the Beaufort Sea shelf and their possible relationship to decomposing methane gas hydrates. Geophysical Research Letters, **34**, no. 1.

Pedrosa, M., A. Camerlenghi, B. De Mol, R. Urgeles, M. Rebesco, and R. Lucchi. 2011, Seabed morphology and shallow sedimentary structure of the Storfjorden and Kveithola trough-mouth fans (North West Barents Sea). Marine Geology, **286**, no. 1,65-81.

Petersen, J., Hustoft, S., Mienert, J., & Buenz, S. (2008, December). High-Resolution 3D Seismic Data Characterize Pockmark and Chimney Structures: Methane Flow Through Hydrated Sediments at the Vestnesa Ridge off the W-Svalbard Margin in the Arctic. In AGU Fall Meeting Abstracts.

Petersen, C. J., S. Bünz, S. Hustoft, J. Mienert, and D. Klaeschen. 2010, High-resolution P-Cable 3D seismic imaging of gas chimney structures in gas hydrated sediments of an Arctic sediment drift. Marine and Petroleum Geology, **27**, no. 9,1981-1994.

Planke, S., F. N. Eriksen, C. Berndt, J. Mienert, and D. Masson. 2009, P-Cable high-resolution seismic. Oceanography, **22**, no. 1,85.

Plaza- Faverola, A., S. Bünz, J. E. Johnson, S. Chand, J. Knies, J. Mienert, and P. Franek. 2015, Role of tectonic stress in seepage evolution along the gas hydrate- charged Vestnesa Ridge, Fram Strait. Geophysical Research Letters, **42**, no. 3,733-742.

Plaza- Faverola, A., G. K. Westbrook, S. Ker, R. J. Exley, A. Gailler, T. A. Minshull, and K. Broto. 2010, Evidence from three- dimensional seismic tomography for a substantial accumulation of gas hydrate in a fluid- escape chimney in the Nyegga pockmark field, offshore Norway. Journal of Geophysical Research: Solid Earth, **115**, no. B8.

Portnov, A., S. Vadakkepuliyambatta, J. Mienert, and A. Hubbard. 2016, Ice-sheet-driven methane storage and release in the Arctic. Nature communications, **7**,10314.

Prosser, S. 1993, Rift-related linked depositional systems and their seismic expression. Geological Society, London, Special Publications, **71**, no. 1,35-66.

Rasmussen, T. L., E. Thomsen, M. A. Ślubowska, S. Jessen, A. Solheim, and N. Koç. 2007, Paleoceanographic evolution of the SW Svalbard margin (76 N) since 20,000 14 C yr BP. Quaternary Research, **67**, no. 1,100-114.

Rebesco, M., J. Laberg, M. Pedrosa, A. Camerlenghi, R. Lucchi, F. Zgur, and N. Wardell. 2014, Onset and growth of trough-mouth fans on the north-western Barents Sea margin–implications for the evolution of the Barents Sea/Svalbard ice sheet. Quaternary Science Reviews, **92**,227-234.

Roy, S., M. Hovland, R. Noormets, and S. Olaussen. 2015, Seepage in Isfjorden and its tributary fjords, West Spitsbergen. Marine Geology, **363**,146-159.

Ruppel, C. 2011, Methane hydrates and contemporary climate change. Nature Education Knowledge, **3**, no. 10.

Ruppel, C. D., and J. D. Kessler. 2017, The interaction of climate change and methane hydrates. Reviews of Geophysics, **55**, no. 1,126-168.

Sahling, H., M. Römer, T. Pape, B. Bergès, C. dos Santos Fereirra, J. Boelmann, P. Geprägs, M. Tomczyk, N. Nowald, and W. Dimmler. 2014, Gas emissions at the continental margin west of Svalbard: mapping, sampling, and quantification. Biogeosciences, **11**, no. 21.

Sarkar, S., C. Berndt, T. A. Minshull, G. K. Westbrook, D. Klaeschen, D. G. Masson, A. Chabert, and K. E. Thatcher. 2012, Seismic evidence for shallow gas- escape features associated with a retreating gas hydrate zone offshore west Svalbard. Journal of Geophysical Research: Solid Earth, **117**, no. B9.

Sen, A., E. K. Åström, W.-L. Hong, A. Portnov, M. Waage, P. Serov, M. L. Carroll, and J. Carroll. 2018, Geophysical and geochemical controls on the megafaunal community of a high Arctic cold seep. Biogeosciences Discuss, **2018**,1-52.

Serié, C., M. Huuse, and N. H. Schødt. 2012, Gas hydrate pingoes: Deep seafloor evidence of focused fluid flow on continental margins. Geology, **40**, no. 3,207-210.

Serov, P., A. Portnov, J. Mienert, P. Semenov, and P. Ilatovskaya. 2015, Methane release from pingo- like features across the South Kara Sea shelf, an area of thawing offshore permafrost. Journal of Geophysical Research: Earth Surface, **120**, no. 8,1515-1529.

Serov, P., S. Vadakkepuliyambatta, J. Mienert, H. Patton, A. Portnov, A. Silyakova, G. Panieri, M. L. Carroll, J. Carroll, and K. Andreassen. 2017, Postglacial response of Arctic Ocean gas hydrates to climatic amelioration. Proceedings of the National Academy of Sciences,201619288.

Shipley, T. H., M. H. Houston, R. T. Buffler, F. J. Shaub, K. J. McMillen, J. W. Ladd, and J. L. Worzel. 1979, Seismic evidence for widespread possible gas hydrate horizons on continental slopes and rises. AAPG bulletin, **63**, no. 12,2204-2213.

Shlykova, V. V., G. S. Kazanin, S. P. Pavlov, A. V. Stupakova, P. O. Golinchik, and P. A. Safronova. 2008, Seismostratigraphic characterization of sedimentary cover of the South Spitsbergen shelf and its hydrocarbon potential. Prospecting and protection of subsoil, **8**,39-44.

Sloan Jr, E. D., and C. Koh. 2007, Clathrate hydrates of natural gases: CRC press.

Solheim, A., and A. Elverhøi. 1993, Gas-related sea floor craters in the Barents Sea. Geo-Marine Letters, **13**, no. 4,235-243.

Solheim, A., and Y. Kristoffersen. 1984, Physical Environment, Western Barents Sea 1: 1,500,000: Norsk polarinstitutt.

Somoza, L., R. León, T. Medialdea, L. F. Pérez, F. J. González, and A. Maldonado. 2014, Seafloor mounds, craters and depressions linked to seismic chimneys breaching fossilized diagenetic bottom simulating reflectors in the central and southern Scotia Sea, Antarctica. Global and Planetary Change, **123**,359-373.

Steinle, L., C. A. Graves, T. Treude, B. Ferré, A. Biastoch, I. Bussmann, C. Berndt, S. Krastel, R. H. James, and E. Behrens. 2015, Water column methanotrophy controlled by a rapid oceanographic switch. Nature Geoscience, **8**, no. 5,378.

Sultan, N., M. Voisset, T. Marsset, A.-M. Vernant, E. Cauquil, J. Colliat, and V. Curinier. 2007, Detection of free gas and gas hydrate based on 3D seismic data and cone penetration testing: An example from the Nigerian Continental Slope. Marine Geology, **240**, no. 1-4,235-255.

Sun, X., G. Waghorn, S. Hoskin, S. Harrison, S. Muetzel, and D. Pacheco. 2012, Methane emissions from sheep fed fresh brassicas (Brassica spp.) compared to perennial ryegrass (Lolium perenne). Animal Feed Science and Technology, **176**, no. 1-4,107-116.

Thatcher, K., G. Westbrook, S. Sarkar, and T. Minshull. 2013, Methane release from warming- induced hydrate dissociation in the West Svalbard continental margin: Timing, rates, and geological controls. Journal of Geophysical Research: Solid Earth, **118**, no. 1,22-38.

Tóth, Z., V. Spiess, J. M. Mogollón, and J. B. Jensen. 2014, Estimating the free gas content in Baltic Sea sediments using compressional wave velocity from marine seismic data. Journal of Geophysical Research: Solid Earth, **119**, no. 12,8577-8593.

Vadakkepuliyambatta, S., S. Bünz, J. Mienert, and S. Chand. 2013, Distribution of subsurface fluid-flow systems in the SW Barents Sea. Marine and Petroleum Geology, **43**,208-221.

Vadakkepuliyambatta, S., S. Chand, and S. Bünz. 2017, The history and future trends of ocean warming-induced gas hydrate dissociation in the SW Barents Sea. Geophysical Research Letters, **44**, no. 2,835-844.

Vorren, T. O., Richardsen, G., Knutsen, S. M., & Henriksen, E. (1991). Cenozoic erosion and sedimentation in the western Barents Sea. Marine and petroleum geology, 8(3), 317-340.

Waghorn, K. A., Pecher, I., Strachan, L. J., Crutchley, G., Bialas, J., Coffin, R., ... & Sarkar, S. (2018). Paleo-fluid expulsion and contouritic drift formation on the Chatham Rise, New Zealand. Basin Research, 30(1), 5-19.Wallmann, K., M. Riedel, W.-L. Hong, H. Patton, A. Hubbard, T. Pape, C. Hsu, C. Schmidt, J. E. Johnson, and M. Torres. 2018, Gas hydrate dissociation off Svalbard induced by isostatic rebound rather than global warming. Nature communications, **9**, no. 1,83.

Wenau, S., Spieß, V., Pape, T., Fekete N. 2017, Controlling mechanisms of giant deep water pockmarks in the Lower Congo Basin, Marine and Petroleum Geology, Volume 83, Pages 140-157, ISSN 0264-8172, https://doi.org/10.1016/j.marpetgeo.2017.02.030.

Westbrook, G. K., K. E. Thatcher, E. J. Rohling, A. M. Piotrowski, H. Pälike, A. H. Osborne, E. G. Nisbet, T. A. Minshull, M. Lanoisellé, and R. H. James. 2009, Escape of methane gas from the seabed along the West Spitsbergen continental margin. Geophysical Research Letters, **36**, no. 15.

Winsborrow, M. C., K. Andreassen, G. D. Corner, and J. S. Laberg. 2010, Deglaciation of a marine-based ice sheet: Late Weichselian palaeo-ice dynamics and retreat in the southern Barents Sea reconstructed from onshore and offshore glacial geomorphology. Quaternary Science Reviews, **29**, no. 3-4,424-442.

Åström, E. K., P. G. Oliver, and M. L. Carroll. 2017, A new genus and two new species of Thyasiridae associated with methane seeps off Svalbard, Arctic Ocean. Marine Biology Research, **13**, no. 4,402-416.
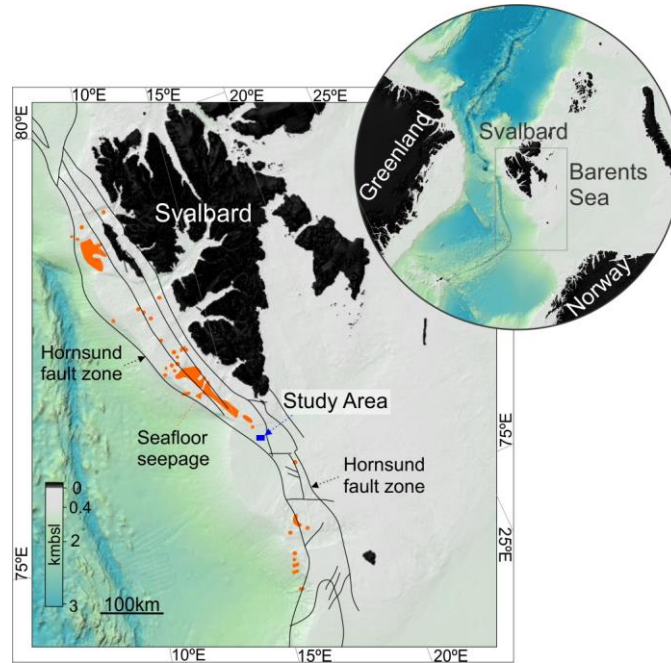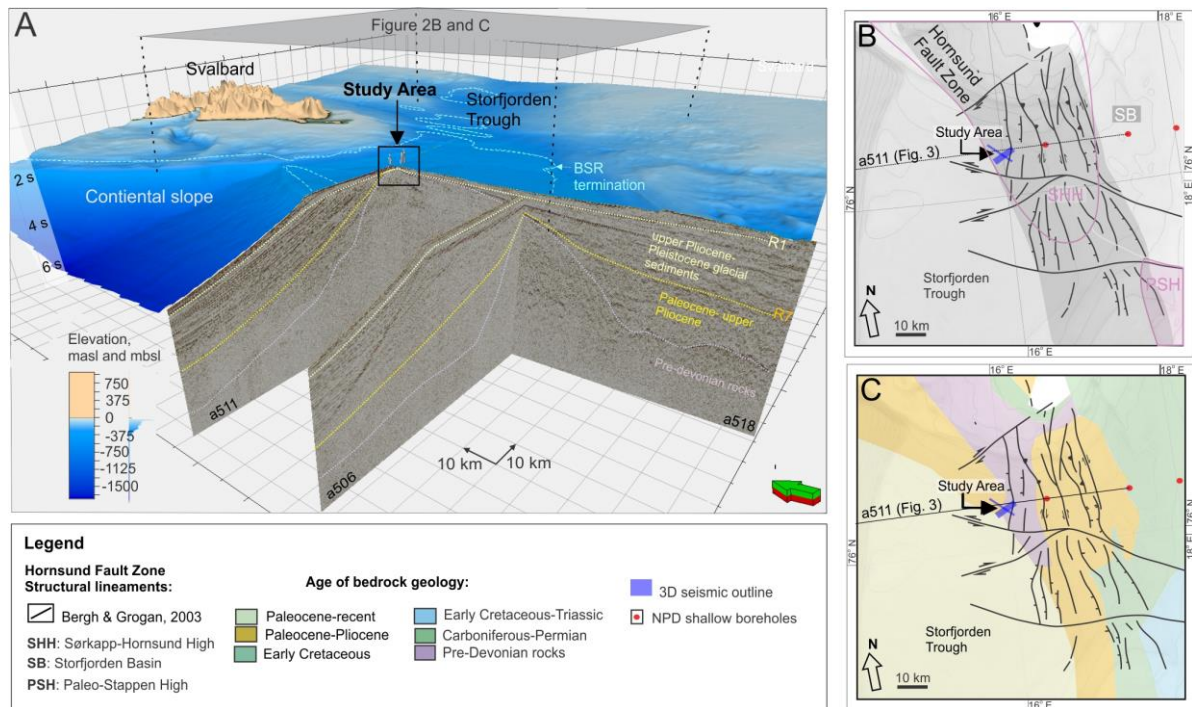
Figure 1. The study area is located in the outer part of the Storfjordrenna Trough, northern Barents Sea, about 50 km south of the southern tip of Svalbard. The Hornsund fault zone strikes along the western Svalbard shelf and northwestern Barents Sea through the study area. Along it, more than 1000 seafloor gas seepage sites exist (orange dots). Flare locations are derived from Mau et al., 2017, whereas fault lineaments from the NPD FactMaps 2.0 (available at http://gis.npd.no/ogc/factmaps/2_0 NPD).
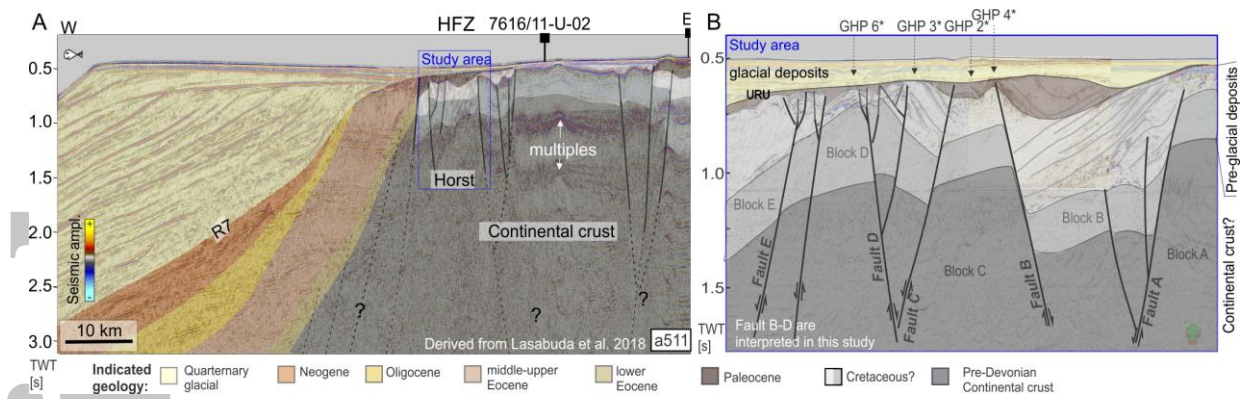
Figure 2. Overview of the study area. A. Seafloor topography of the Storfjordrenna and regional seismic lines showing Paleocene-Pleistocene deposits and underlying basement high (Sørkapp Hornsund High). The black square indicates the study area. B. Regional structures (Bergh and Grogan., 2003), and location of basement highs and lows (Anell et al., 2016). In C. bedrock geology underneath the upper glacial package (Dallmann, 2015). On inset B and C, the blue transparent area indicate the location of the 3D seismic cubes, the red dots the location of shallow NPD boreholes, and the line crossing the study area and boreholes is seismic line a511 presented in figure 3.

Figure 3. A MAGE (Murmansk Arctic Geological Expedition) 2D seismic line (a511) across the study area (location in figure 2B and C) with interpreted geology, deep-seated faults and GHPs (*arrows indicate approximate location, following the underlying structural lineaments). The structural elements and geology are interpreted by Lasabuda et al. (2018). The insert B show a close up of the approximate study area. Here, the Cenozoic (glacial and pre-glacial) sedimentary package drastically thins. Above the Pre-Devonian basement, some Cretaceous rocks are possible present underneath basin-confined Palaeocene sedimentary rocks, and above; only a relatively thin drape of Quaternary glacial deposits. The west and east dipping normal faults divide the section into grabens and half grabens, which accommodate the Palaeocene basins between more elevated horsts.
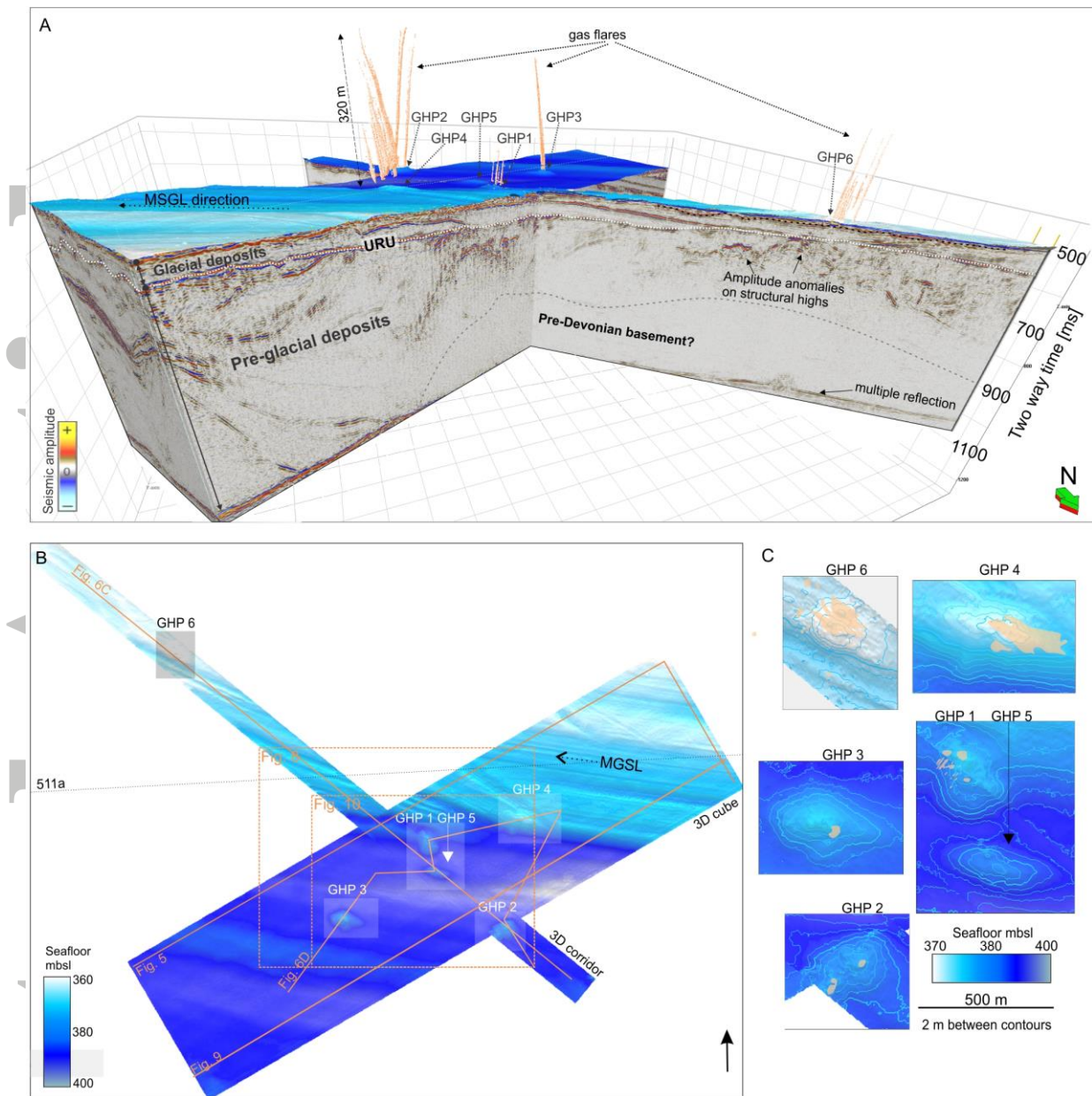
Figure 4. Two 3D seismic cubes and acoustic flare data used in this study. A. The 3D seismic volumes show the GHPs and mega scale glacial lineations (MGSL) on the seafloor, and beneath; two seismo-stratigraphic units - the upper "glacial deposits" and the lower "pre-glacial deposits". Little to no seismic energy characterizes the lowermost part, which may be indicative to be upper part of the pre-Devonian basement. B. Show a map view of the depth converted seismic bathymetry. C. Close-up of the gas hydrate pingos with flare locations (light orange color).
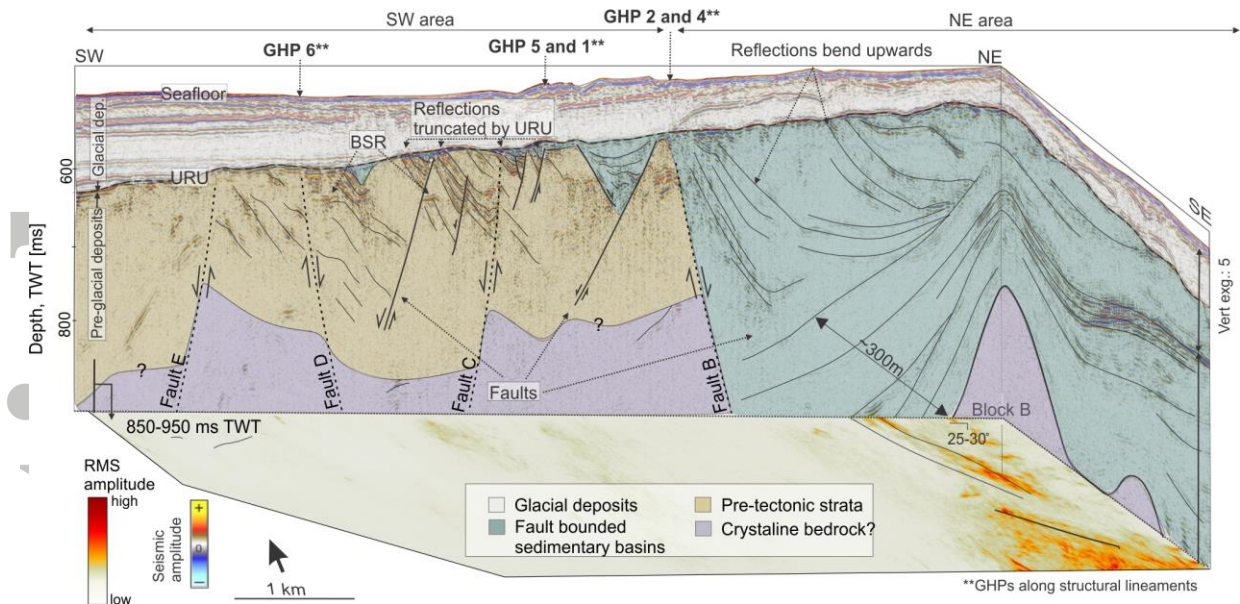
Figure 5. Fragment of 3D cube showing acoustic highs with no internal seismic reflections (loss of seismic signal) and structural components of the pre-glacial deposits combined with an RMS amplitude map for 850- 950 ms interval TWT highlighting amplitude anomalies associated with the structure.
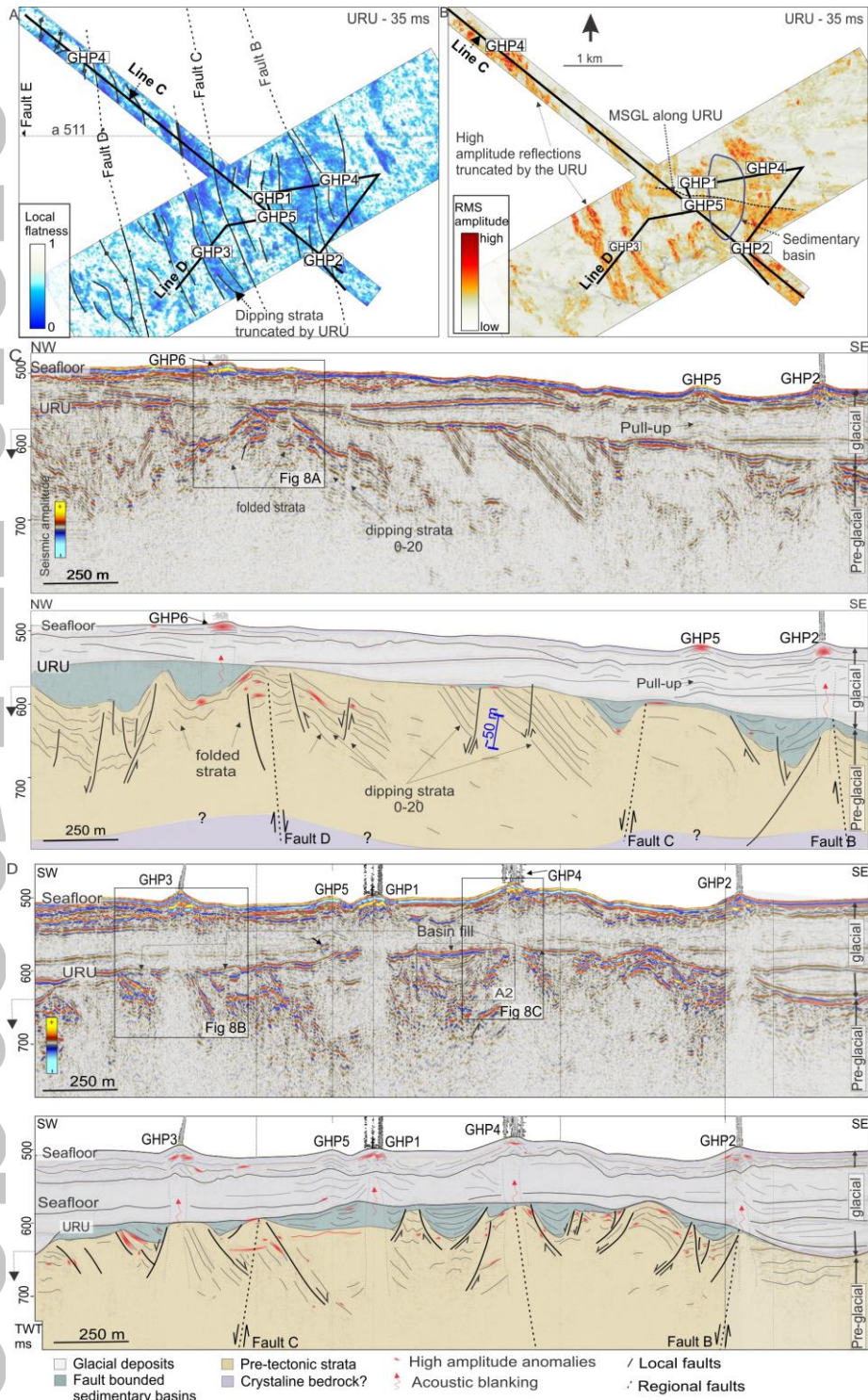
Figure 6: Seismic examples of the glacial and the pre-glacial deposits from the 3D cubes. A. Flatness map and B. RMS amplitude map of strata between URU and 35 ms TWT below it, showing dipping events that are truncated by URU and high amplitude seismic anomalies within the upper part of the pre-glacial deposits. C. show a seismic line across the Storfjordrenna Corridor and below, D. a composite line of the Storfjordrenna 3D. Both lines indicate location of GHPs and underlying geological structures.
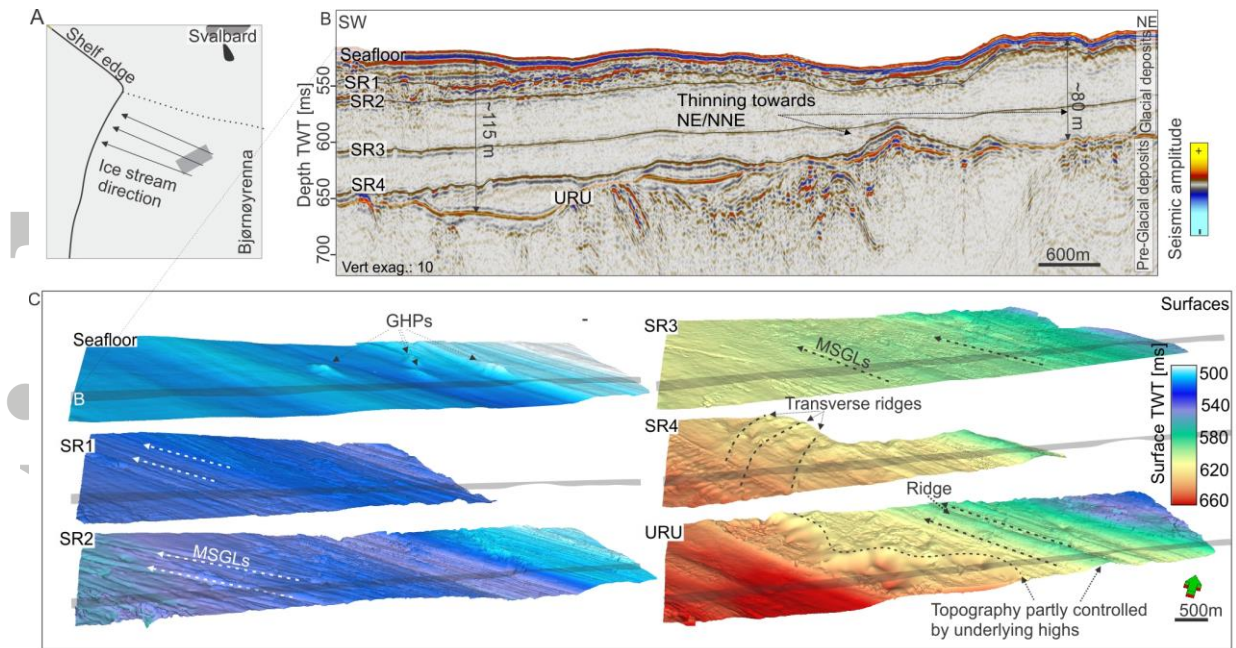
Figure 7. Geomorphological characteristics of the seafloor and the glacial deposits. A. The direction of former ice flow towards the northwestern Barents Sea shelf edge. B. seismic cross-section showing the location of SR1, SR2, SR3, SR4, and URU (location of line in Figure 3) along the 3D seismic cube. The glacial unit thins towards NNE/NE. C. Surface maps of the seafloor, SR1-SR4 and URU. SR1-4 and URU is dominated by MSGLs, transverse ridges and rough topography, whereas the seafloor is the only surface showing additional positive mounds (GHPs). The dark shaded line (as well as Figure 4B) on the surfaces indicates the location of the seismic example (B).
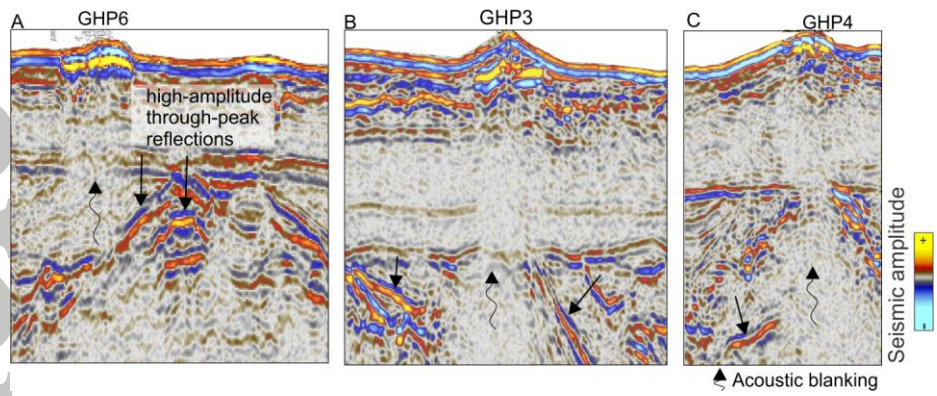
Figure 8. Close up of seismic beneath GHP6 (A), GHP3 (B) and GHP4 (C) showing high-amplitude anomalies of trough-peak reflection indicating a transition to a lower acoustic impedance material such as gas-bearing sedimentary rocks. Location of inset in figure 6C and D.
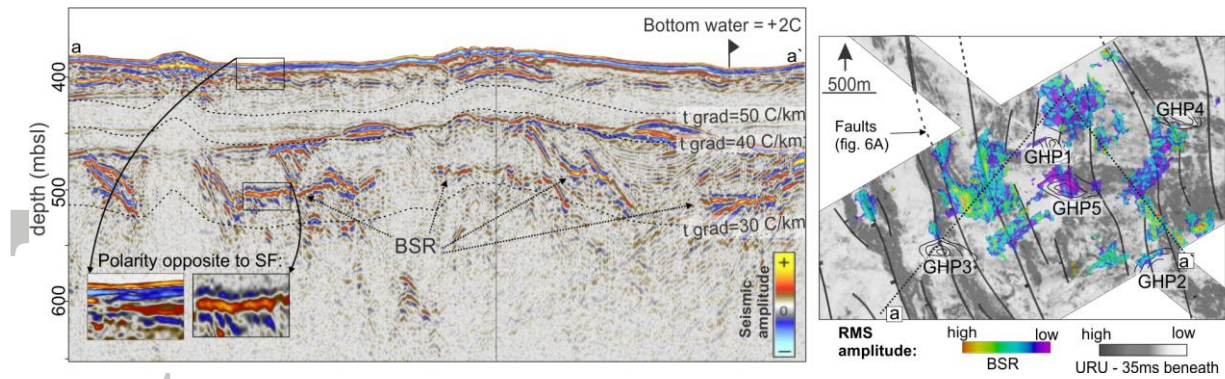
Figure 9. Seismic example (a-a`) of the observed BSR and modeled results using 30, 40 and 50 C/km thermal gradient. Insert shows amplitude of- and BSR distribution across the study area. Countors indicate the location of GHPs 1-5. MBSL is here used instead of TWT for comparison with the GHSZ modelling results. Location of map insert in figure 4B.
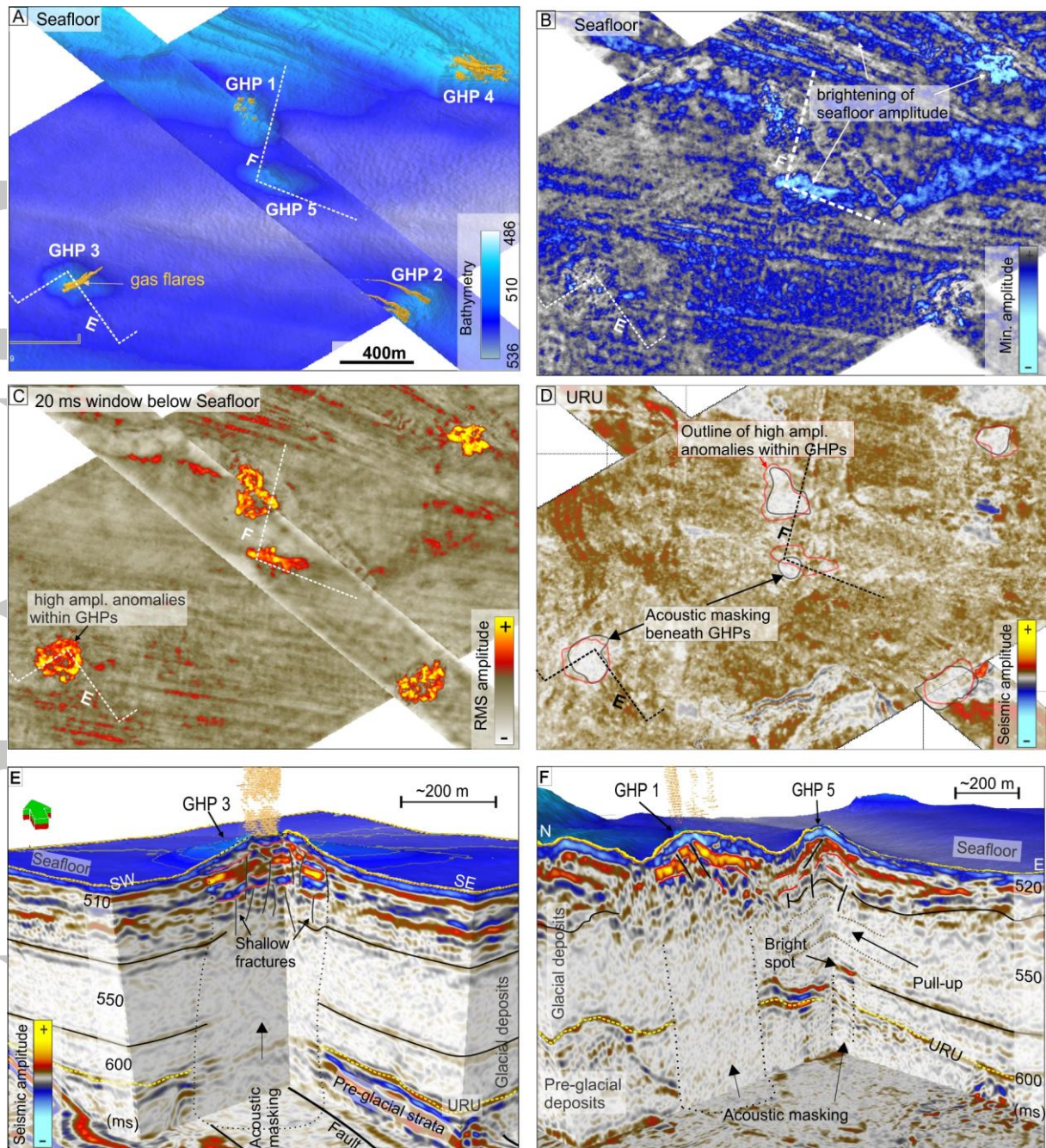
Figure 10. Seismic characteristics of the GHPs and shallow fluid flow anomalies. A: Seafloor bathymetry and location of GHPs and gas flares; B: Minimum amplitude of seafloor reflection presenting amplitude variations across GHPs. As seen, GHP 1, 5 and 4 show high amplitude anomalies, while GHP 3 and partly 2 show little variation in amplitude compared to surrounded seafloor; C: RMS amplitude map of a 20 ms window beneath the seafloor reflection, highlighting high amplitude anomalies beneath the shallow surface of all GHPs; D: seismic reflection along URU indicating areas of acoustic masking beneath GHPs (grey outline). For comparison, the outline of the location of the high amplitude anomalies in C are drawn on the map (red outline), E, F: 3D view of GHP 3, 1 and 5 with seismic time-slice of the upper pre-glacial deposits, showing the areas of acoustic masking through the glacial deposits and amplitude anomalies within GHPs. Locations of the seismic in relation of the attribute maps is shown in A-D.
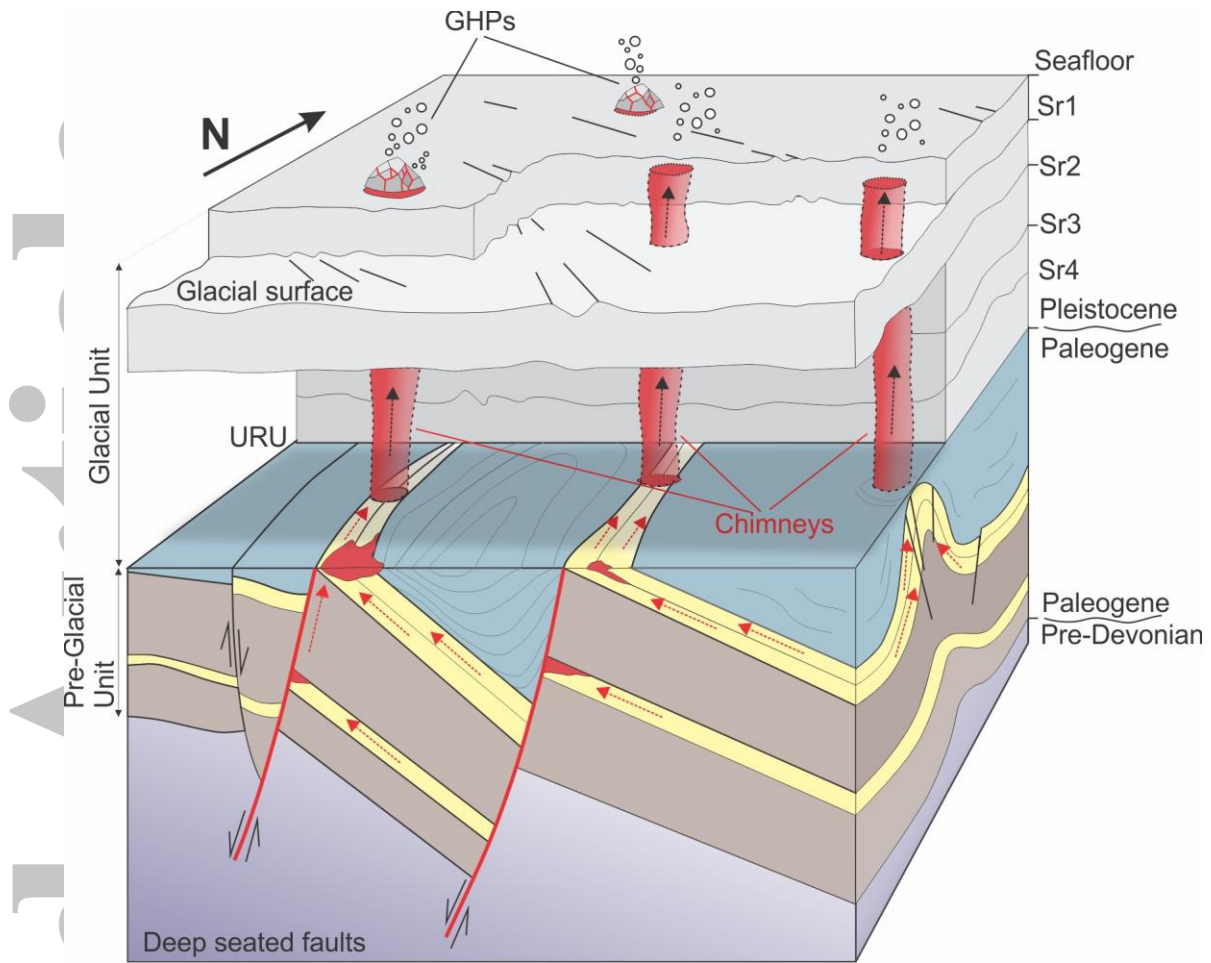
Figure 11. Conceptual model of the fluid flow and gas hydrate system of the Storfjordenna GHP site. We suggest subsurface gas migration occurs through faults and permeable inclined bedding of the pre-glacial deposits, and through a sub-vertically fracture networks (gas chimneys) of the low-permeable glacial deposits beneath the seafloor pingos. Precipitation of autogenic carbonate and hydrate growth causes sediments to decrease in bulk density and expand forming gas hydrate pingos on the seafloor.
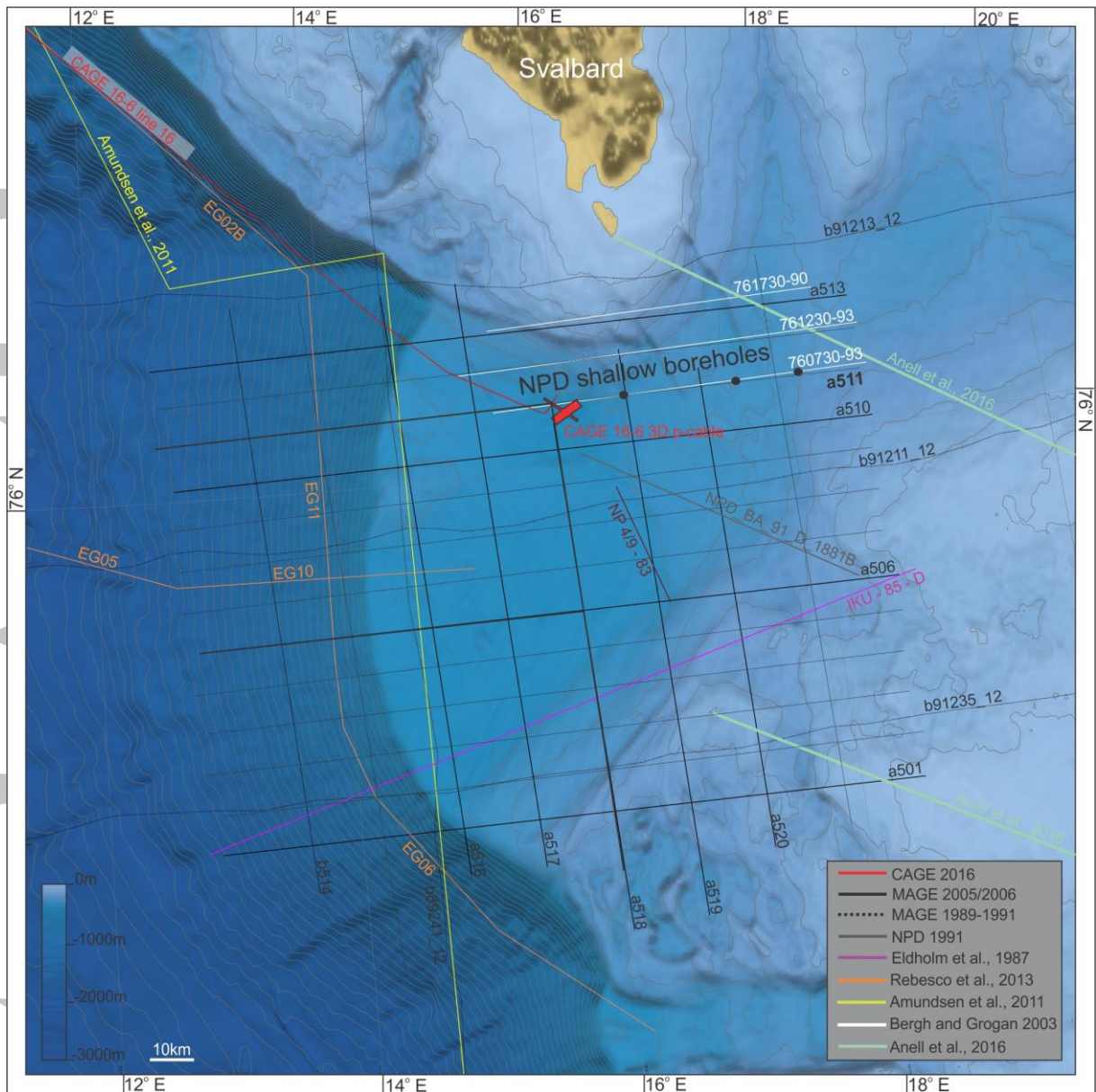
Figure A2. Slightly asymmetric layered sedimentary basin inferred to be confined by faulted margins. Location in figure

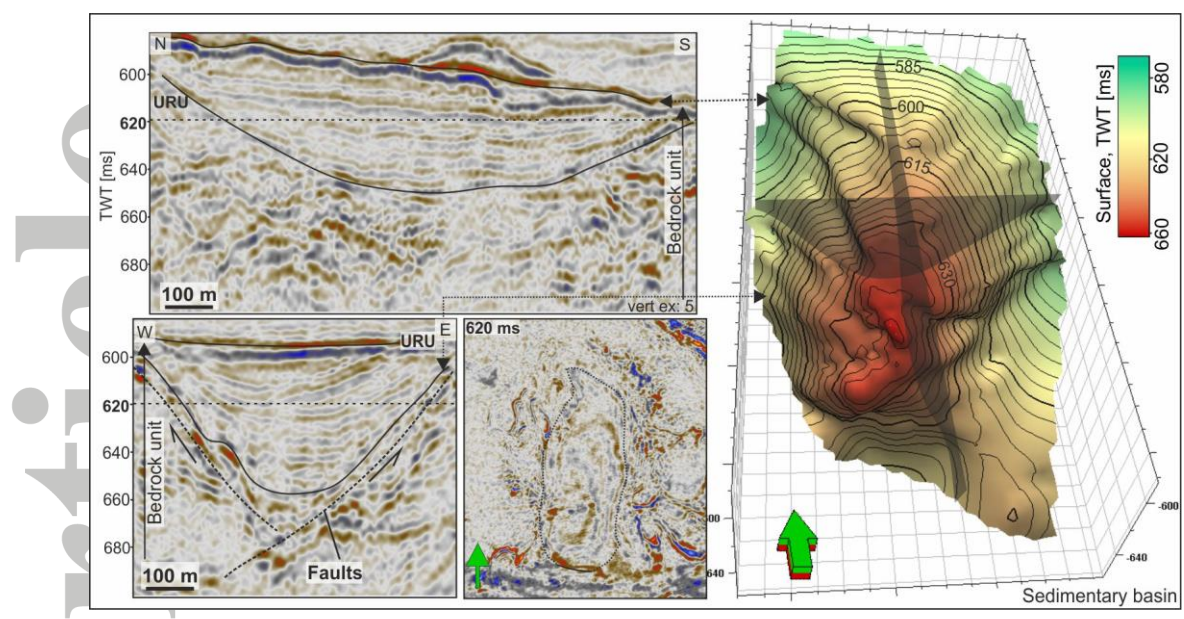**Figure A1.** Overview of data used in the study for seismic correlation and unit characterization.